

Segmentation of Bone Structures in X-ray Images

Thesis Proposal
Submitted to School of Computing

by

Ding Feng (HT040297J)

under guidance of

Dr. Leow Wee Kheng (Associate Professor)

School of Computing
National University of Singapore

July 2006

Abstract

Medical image segmentation, as an application of image segmentation, is to extract anatomical structures from medical images. In this thesis proposal, existing methods for medical image segmentation are reviewed. According to the review, segmentation of multiple bone structures in complex x-ray images is not well studied. This leads to the proposed research topic: segmentation of bone structures in x-ray images. Atlas-based segmentation is a promising approach for solving such a complex segmentation problem. Preliminary work on atlas-based segmentation of CT and x-ray images suggests that this approach can provide a robust and accurate method for automatic segmentation of x-ray images.

Acknowledgement

I want to thank my supervisor, A/Professor Leow Wee Kheng, who gave me invaluable advice for writing this term paper.

I also thank Ruixuan Wang, Piyush Kanti Bhunre Dennis Lim Shere, Ying Chen, Xiaoping Miao and Sheng Zhang for their precious comments and suggestions.

List of Figures

1.1	Hip replacement.	2
2.1	Thresholding of image with bimodal intensity distribution.	5
2.2	Thresholding of image with multi-modal intensity distribution.	6
2.3	Adaptive thresholding.	6
2.4	Canny edge detection result.	7
2.5	Seeded region growing segmentation.	9
2.6	Model of the watershed algorithm.	10
2.7	Sample result of the watershed algorithm.	10
2.8	Bone removal in a CT image.	12
2.9	Fuzzy membership functions.	13
2.10	Snake segmentation of bone.	14
2.11	Gradient vector flow.	15
2.12	Merging of contours.	16
2.13	Level set segmentation of heart image.	17
2.14	Segmentation of cartilage by active shape model.	18
2.15	Iterative corresponding point.	22
2.16	Attraction vs. diffusion methods.	24
2.17	PASHA vs. demons algorithm.	25

2.18	Level set algorithm applied to neck axial slice.	25
2.19	Pixel classification.	26
2.20	Heart intensity distribution.	27
2.21	Region-based wrist x-ray image segmentation.	28
2.22	Thresholding based on fuzzy index measure.	29
2.23	Initialization of tooth contour extraction.	30
2.24	Segmentation result of femur.	31
2.25	Geometrical model.	33
2.26	Geometric model based lung segmentation.	34
2.27	Active shape model-based segmentation of hip images.	35
2.28	Shape context.	36
3.1	Characteristics of x-ray images.	38
3.2	Representation of the pelvis bone.	39
3.3	Sample pelvis x-ray images.	40
4.1	Atlas contours.	43
4.2	Iterative local transformation.	45
4.3	Sample results after refinement.	46
4.4	Test results.	47
4.5	Pelvis x-ray images.	48
4.6	Edge extraction.	49
4.7	Global alignment algorithm.	50
4.8	Registration of atlas contour to different edge segments in an input image.	52
4.9	Sample good results of global alignment.	53
4.10	Sample poorer results of global alignment.	54

Contents

ABSTRACT	i
ACKNOWLEDGEMENT	ii
LIST OF FIGURES	iii
1 Introduction	1
1.1 Motivation	1
1.2 Organization of the Paper	3
2 Literature Review	4
2.1 General Medical Image Segmentation Methods	4
2.1.1 Thresholding	4
2.1.2 Edge-based	6
2.1.3 Region-based	7
2.1.4 Graph-based	9
2.1.5 Classification-based	12
2.1.6 Deformable Model	13
2.1.7 Summary	19
2.2 Atlas-based Segmentation Methods	20
2.2.1 Global Alignment	20

2.2.2	Local Refinement	22
2.2.3	Summary	27
2.3	Segmentation of X-ray Images	28
2.3.1	Region-based	29
2.3.2	Classification-based	29
2.3.3	Deformable Model	30
2.3.4	Geometric Model	32
2.3.5	Atlas-based Method	33
2.3.6	Summary	34
3	Proposed Research Topic	37
3.1	Problem Analysis	37
3.2	Problem Formulation	39
3.3	Research Plan	41
4	Preliminary Work	42
4.1	Segmentation of Soft Tissues in Abdominal CT Images	42
4.1.1	Global Alignment	42
4.1.2	Iterative Local Deformation	43
4.1.3	Local Refinement	45
4.1.4	Experiments and Discussion	45
4.2	Global Alignment of Bone Structures in Pelvis X-ray Images	47
4.2.1	Segmentation Algorithm	47
4.2.2	Experiments and Discussion	50
5	Conclusions	55

BIBLIOGRAPHY

57

Chapter 1

Introduction

1.1 Motivation

There exist many types of x-ray images, such as normal x-ray images, angiograms, x-ray microscopic images, mammography images and fluroscopic images, etc. Certain types of x-ray images, such as angiograms, are obtained by inserting contrast agent into the patient's blood to enhance the contrast between the blood vessels and their neighboring tissues. Normal x-ray images of the bone are the most commonly used imaging modality for doctors to diagnose and treat bone diseases. Some examples of the use of x-ray images are as follows:

- Fracture diagnosis and treatment. X-ray images are most frequently used in fracture diagnosis because it is the fastest and easiest way for the doctors to study the injuries of bones and joints. Doctors usually use x-ray images to determine whether a fracture exists, and the location of the fracture. In the recovery process, doctors also use x-ray images to determine whether the injured bones and joints have recovered.
- Evaluation of skeletal maturation. X-ray images are used to determine the physiological age and growth potential, and to predict adult stature.
- Bone densitometry. Bone densitometry measures the calcium content in the bones. In general, people with bone mineral densities significantly lower than the normal level are more likely to break a bone. Bone densitometry does not indicate whether bone fractures exist or not, but can predict the risk of fracture occurrence.



Figure 1.1: Hip replacement. The patient's right hip (on the left in the photograph) has been replaced by a metal implant (http://en.wikipedia.org/wiki/Hip_replacement).

- Hip replacement. Hip replacement is a medical procedure in which the hip joint is replaced with a metal implant, and the hip socket is replaced with a plastic or a metal and plastic cup. Hip replacement surgery requires x-ray images of the hip.

In all the medical applications highlighted above, segmentation of bones in x-ray images is an important step in computer-aided diagnosis, surgery and treatment.

There are three general approaches for medical image segmentation, namely, manual segmentation, semi-automatic segmentation and automatic segmentation. They all have their pros and cons. Manual segmentation by domain experts is the most accurate but time-consuming. Semi-automatic segmentation requires the user to provide a small amount of inputs to facilitate accurate segmentation. Automatic segmentation does not require any user input and, thus, is much more difficult to obtain accurate results. Nevertheless, in many applications that involve a large number of images, it is the only practically feasible approach. Therefore, the main focus of this research is on automatic segmentation.

1.2 Organization of the Paper

The rest of this paper is organized as follows. Chapter 2 includes a literature review covering some existing medical image segmentation algorithms and their strengths and weaknesses. Based on the literature review, the research topic is proposed in Chapter 3. Some preliminary research and the experimental results are described in Chapter 4 and Chapter 5 concludes the paper.

Chapter 2

Literature Review

This review begins with general medical image segmentation methods (Section 2.1), which usually cannot be used alone to segment complex medical images. Next, a more advanced approach called the atlas-based approach that can incorporate domain knowledge is reviewed (Section 2.2). Finally, existing methods for the segmentation of x-ray images are reviewed (Section 2.3).

2.1 General Medical Image Segmentation Methods

General medical image segmentation methods can be classified into the following categories [1, 2]: *thresholding*, *edge-based*, *region-based*, *classification-based*, *graph-based* and *deformable model*.

2.1.1 Thresholding

Thresholding [3] is one of the basic segmentation techniques. Given an image I , thresholding method tries to find a threshold t such that pixels with intensity values greater than or equal to t are categorized into group 1, and the rest of the pixels into group 2. Thresholding requires that the intensity of the image has a bimodal distribution. The algorithm can perform well on simple images with bimodal intensity distribution (Figure 2.1). However, most of the medical images do not have bimodal distribution of intensity. In this case, thresholding result cannot correctly partition the images into various

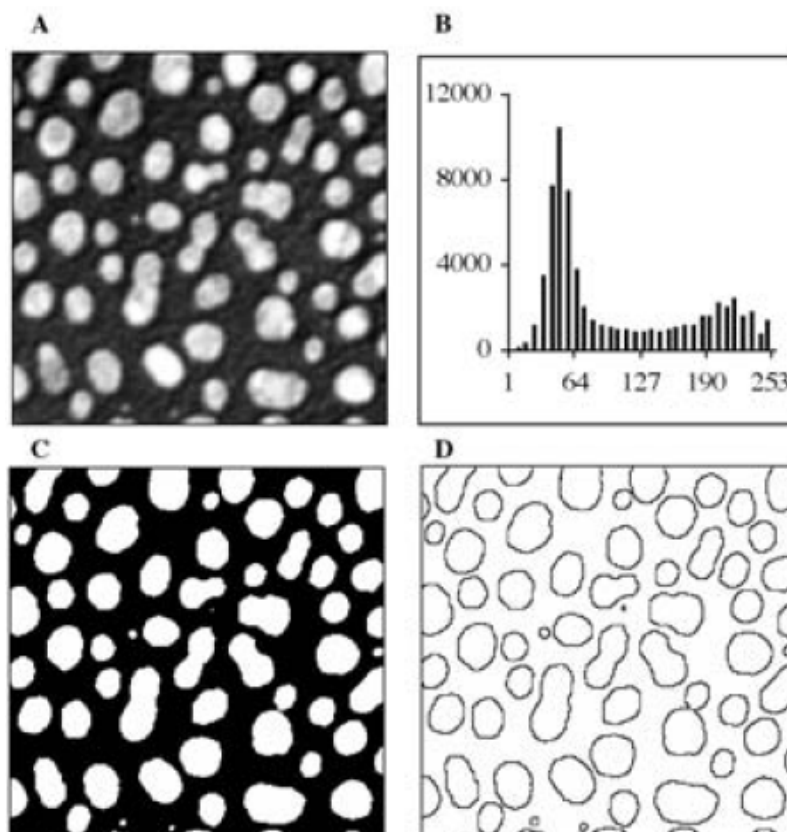


Figure 2.1: Thresholding of image with bimodal intensity distribution, (A) Input image. (B) Intensity histogram of (A). (C) Result of thresholding at $t = 127$. (D) Outlines of the white cells after applying a 3×3 Laplacian to (C) (from [2]).

anatomical structures (Figure 2.2).

Uneven illumination is another factor that affects the performance of thresholding. Adaptive thresholding [4] handles this problem by subdividing an image into multiple sub-images, and applying different thresholds on the sub-images (Figure 2.3). The problem with adaptive thresholding is how to subdivide the image and how to estimate the threshold for each sub-image.

In general, thresholding algorithms do not consider the spatial relationship between pixels. Moreover, the segmentation result is quite sensitive to noise. Thresholding alone is seldom used for medical image segmentation. Instead, it usually functions as an image processing step as in [5].

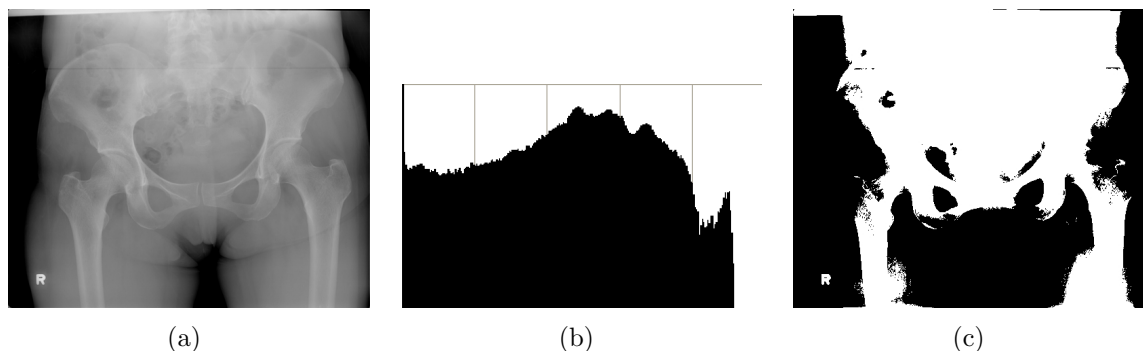


Figure 2.2: Thresholding of image with multi-modal intensity distribution. (a) Input image. (b) Intensity histogram of (a). (c) Result of thresholding at $t = 127$.

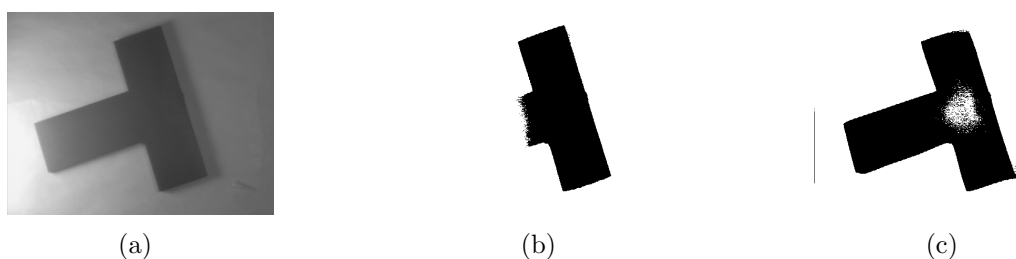


Figure 2.3: Adaptive thresholding. (a) Input image with strong illumination gradient. (b) Result of global thresholding at $t = 80$. (c) Adaptive thresholding using 140×140 window (from <http://homepages.inf.ed.ac.uk/rbf/HIPR2/adpthrsh.htm>).

2.1.2 Edge-based

Edge-based segmentation algorithms use edge detectors to find edges in the image. Traditional *Sobel* edge detector [4] uses a pair of 3-by-3 convolution kernels to compute the first order derivatives (gradients) along the x - and y -directions of the 2-D image. Instead of computing first order derivatives, the *Laplacian* computes the second order derivatives of the image. Usually, the Laplacian is not applied directly on the image since it is sensitive to noise. It is often combined with a Gaussian smoothing kernel, which is referred to as the Laplacian of Gaussian function. Bomans *et al.* [6] used a 3-D extension of Laplacian of Gaussian (LoG) for the segmentation of brain structures in 3-D MR images. Gosh-tasby and Turner [5] used this operator to extract the ventricular endocardial boundary in cardiac MR images.

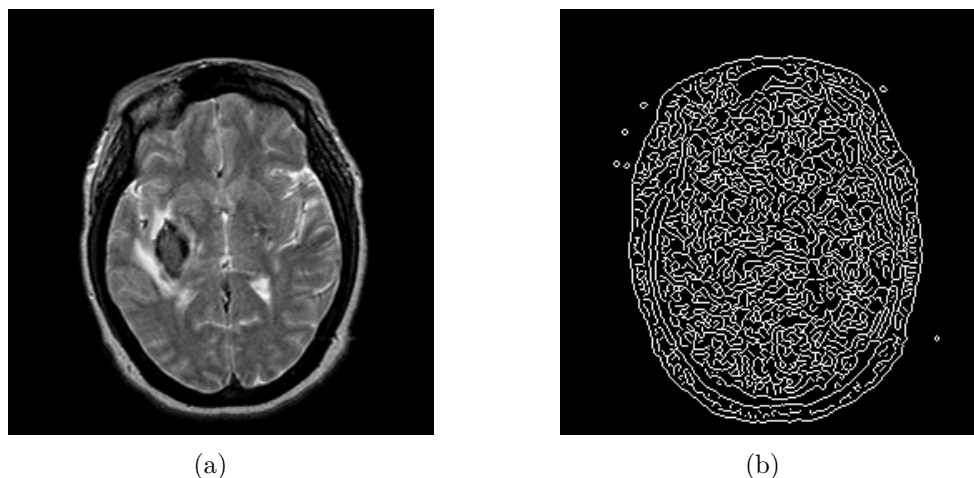


Figure 2.4: Canny edge detection result. (a) Input image. (b) Edge map obtained by Canny edge detector.

More advanced edge detectors have been proposed in the computer vision literature. *Canny* edge detector [7] uses a double-thresholding technique. A higher threshold t_1 is used to detect edges with strict criterion, and a lower threshold t_2 is used to generate a map that helps to link the edges detected in the former step (Figure 2.4). Harris proposed a combined corner and edge detector known as the *Harris* detector [8], which finds the edges based on the eigenvalues of the Hessian matrix.

Edge-based image segmentation algorithms are sensitive to noise and tend to find edges that are irrelevant to the real boundary of the object. Moreover, the edges extracted by edge-based algorithms are disjoint and cannot completely represent the boundary of an object. Additional processing is needed to connect them to form closed and connected object regions.

2.1.3 Region-based

Typical region-based segmentation algorithms include *region growing* and *watershed*.

A. Region Growing

Region growing algorithm begins with selecting n seed pixels. The seed pixel can be selected either manually or by certain automatic procedures, e.g., *converging square* algorithm [9] applied in [10]. Converging square algorithm recursively decomposes an $n \times n$ square image into four $(n-1) \times (n-1)$ square images and chooses the one with maximum intensity density. This procedure is repeated until a single point remains. Each seed pixel i is regarded as a region A_i , $i \in \{1, 2, \dots, n\}$. The algorithm then adds neighboring pixels to the regions with similar image features, thereby growing the regions. The choice of homogeneity criterion is crucial for the success of the algorithm.

A homogeneity criterion proposed by Adams and Bischof [10] is the difference between the pixel intensity and the mean intensity of the region. Yu *et al.* [11] proposed to use the weighted sum of gradient information and the contrast between the region and the pixel as the homogeneity criterion. Pohle and Toennies [12] proposed an adaptive region growing algorithm that incorporated a homogeneity learning process instead of using a fixed criterion.

Region growing algorithms are fast, but may produce undesired segments if the images contain much noise (Figure 2.5). Furthermore, region-based algorithms will segment objects with inhomogeneous region into multiple sub-regions, resulting in over-segmentation.

B. Watershed

The watershed algorithm [13] is another region-based image segmentation approach originally proposed by Beucher and Lantuéjoul. It is a popular segmentation method coming from the field of mathematical morphology. According to Serra [14], the watershed algorithm can be intuitively thought of as a landscape or topographic relief that is flooded by water. The height of the landscape at each point represents the pixel's intensity. Watersheds are the dividing lines of the catchment basins of rain falling over the regions (Figure 2.6). The input of the watershed transform is the gradient of the image, so that the catchment basin boundaries are located at high gradient points [15].

The watershed transform has good properties that make it useful for many image segmentation applications. It is simple and intuitive. It can also be parallelized [15],

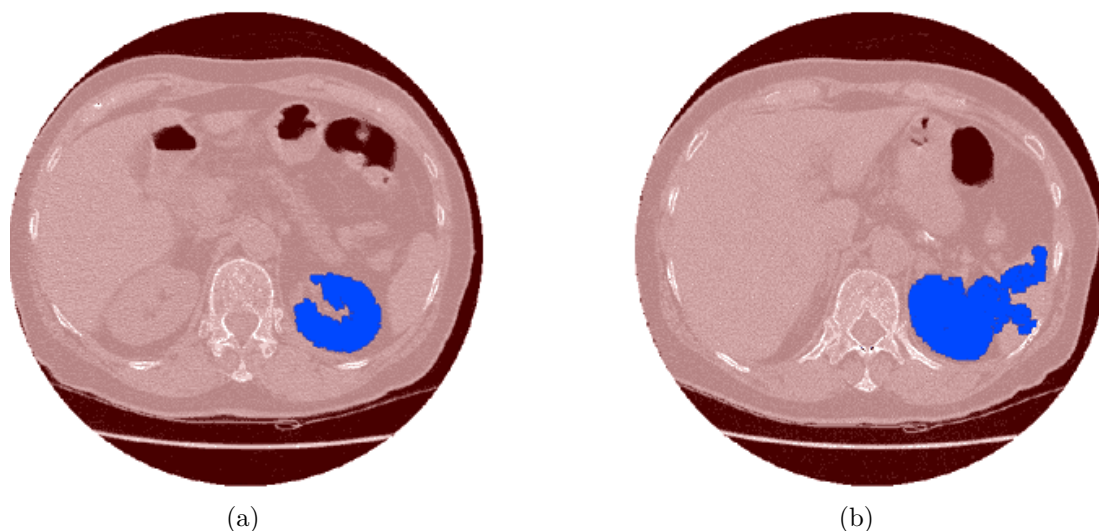


Figure 2.5: Seeded region growing segmentation. (a) A good kidney segmentation result. (b) A bad segmentation result. Some regions are incorrectly merged together (from <http://www.via.cornell.edu/ece547/projects/g3/results.htm>).

and always produces a complete division of the image. However, it has several major drawbacks. It can result in over-segmentation (Figure 2.7) because each local minimum, regardless of the size of the region, will form its own catchment basin. It is also sensitive to noise. Moreover, watershed algorithm is poor at detecting thin structures and structures with low signal-to-noise ratio [16].

To improve the algorithm, Najman and Schmitt proposed to use morphological operations to reduce over-segmentation [17]. Grau *et al.* [16] encoded prior information into the algorithm. Part of its cost function is changed from the gradient between two pixels to the difference of posterior probabilities of having an edge between two pixels given their intensities as the prior information. Wegner *et al.* [18] proposed to perform a second watershed transform on the mosaic image generated by the first watershed transform to reduce over-segmentation.

2.1.4 Graph-based

Graph-based approach is relatively new in the area of image segmentation. The common theme underlying this approach is the formation of a weighted graph, where each vertex

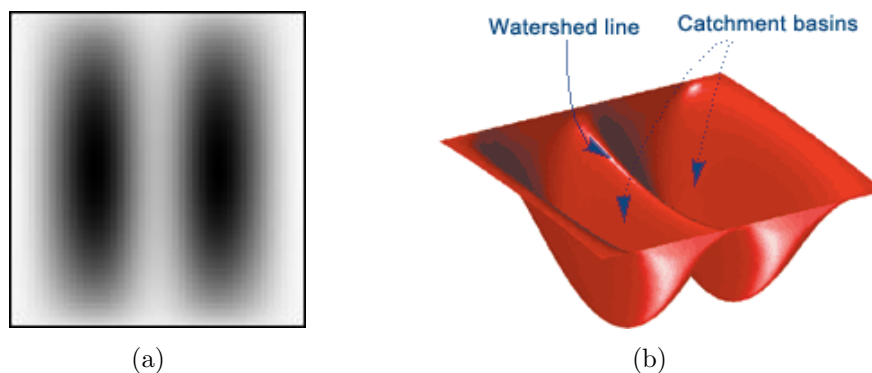


Figure 2.6: Model of the watershed algorithm. (a) The input image and (b) the topological illustration. Regions with low intensities in (a) correspond to the catchment basins in (b), and the region with high intensity is the watershed line (from <http://www.mathworks.com/company/newsletters/newsnotes/win02/watershed.html>).

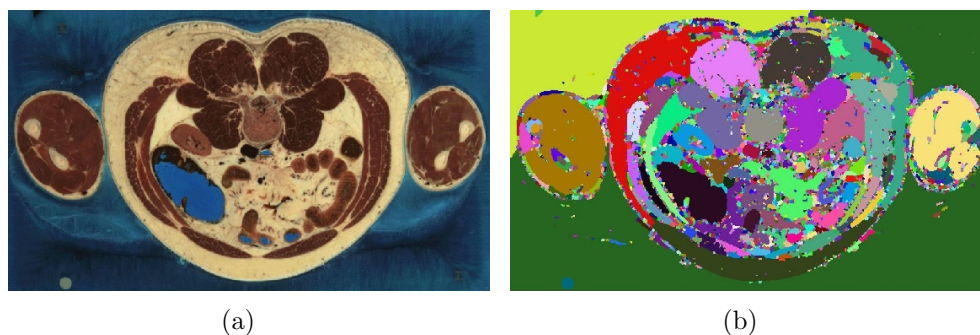


Figure 2.7: Sample result of the watershed algorithm. Over-segmentation is clearly visible. (a) The input image. (b) The segmentation result (from <http://www.itk.org/HTML/WatershedSegmentationExample.html>).

corresponds to an image pixel or region and each edge is weighted with respect to the similarity between pixels or regions. A graph $G = (V, E)$ can be partitioned into two disjoint sets A and B , where $A \cup B = V$ and $A \cap B = \emptyset$, by removing edges between them. Graph-based algorithms try to minimize certain cost functions, such as a *cut*,

$$cut(A, B) = \sum_{u \in A, v \in B} w(u, v) \quad (2.1.1)$$

where $w(u, v)$ is the edge weight between u and v .

Wu and Leahy proposed the *minimum cut* in [19]. A graph is partitioned into k

sub-graphs such that the maximum cut across the subgroups is minimized. However, based on this cutting criterion, their algorithm tends to cut the graph into small sets of nodes because the value of Eqn. (2.1.1) is, to some extent, proportional to the size of the sub-graphs. To avoid this bias, Shi and Malik [20] proposed the *normalized cut* with a new cost function $Ncut$,

$$Ncut(A, B) = \frac{cut(A, B)}{assoc(A, V)} + \frac{cut(A, B)}{assoc(B, V)} \quad (2.1.2)$$

where $assoc(X, V) = \sum_{u \in X, t \in V} w(u, t)$ is the total connection from nodes in X to all nodes in the graph. In [21], Wang and Siskind further improved the graph cut algorithm, and proposed a new cost function for general image segmentation, namely *Ratio Cut*. This scheme finds the minimal ratio of the corresponding sums of two different weights associated with edges along the cut boundary in an undirected graph:

$$Rcut(A, B) = \frac{c_1(A, B)}{c_2(A, B)} \quad (2.1.3)$$

where $c_1(A, B)$ is the first boundary cost that measures the homogeneity of A and B , and $c_2(A, B)$ is the second boundary cost that measures the number of links between A and B . A polynomial-time algorithm is also proposed.

Boykov and Jolly [22] used graph cuts for interactive organ segmentation, e.g., bone removal from abdominal CT images. Their segmentation is initialized with some manual “clicks” and “strokes” on object regions and backgrounds (Figure 2.8). These clicks and strokes are regarded as seed points, which provide information such as hard constraints for the segmentation, and intensity distributions for object and background. The information is later integrated into the proposed graph cut cost function, and the cost function is minimized when segmentation is done. Compared to region-based segmentation algorithms, graph-based segmentation algorithms tend to find the global optimal solutions, while region-based algorithms are based on greedy search. Since graph-based algorithms try to find the global optimum, it is computationally expensive. Over-segmentation is also one of the problems since it uses low-level features such as intensity and edges, which are often corrupted by noise.

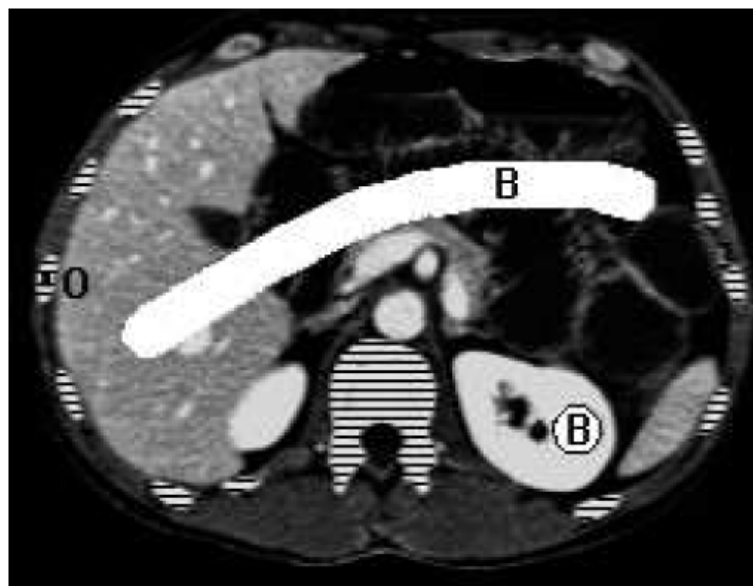


Figure 2.8: Bone removal in a CT image using interactive graph cut [22]. The regions marked by “O” and “B” are manually initialized as object and background respectively. Bone segments are marked by horizontal lines.

2.1.5 Classification-based

Ren and Malik proposed to train a classifier to classify “good segmentation” and “bad segmentation” [23]. The criteria used for the classification include texture similarity, brightness similarity, contour energy, curvilinear continuity, etc. A preprocessing step which groups pixels into “superpixels” is used to reduce the size of the image. This step is actually done by applying the normalized cut algorithm [20]. Human segmented natural images are used as positive examples, while negative examples are constructed by randomly matching human segmentations and the images.

Fuzzy reasoning methods are proposed to detect the cardiac boundary automatically [24, 25]. These methods begin with the application of the Laplacian-of-Gaussian to obtain the zero-crossing areas of the image. High-level knowledge is usually represented in linguistic form. For example, intensities are described as “dark”, “dim”, “medium bright” or “bright”. Fuzzy sets are developed based on the fuzzy membership functions of these linguistic categories (Figure 2.9). The fuzzy membership function is set empirically to describe the range of possible intensity values. A rough boundary region is then obtained

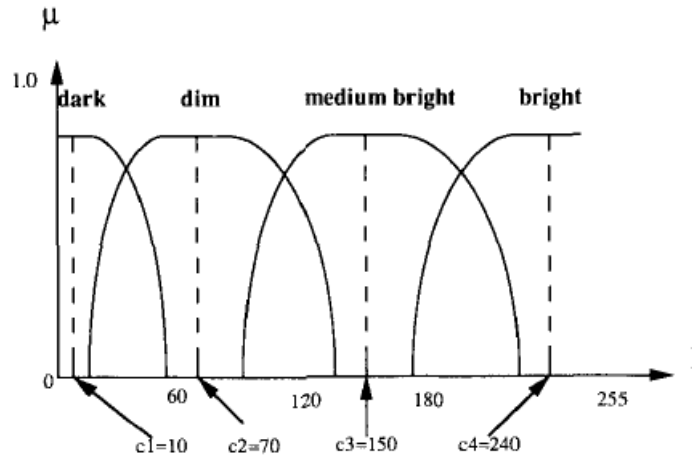


Figure 2.9: Fuzzy membership functions for linguistic descriptions *dark*, *dim*, *medium-bright* and *bright* [25], c_1 – c_4 are the intensity values at which the respective membership function reaches its maximum.

from fuzzy reasoning, where a search operation is employed to obtain the final boundary.

Toulson and Boyce proposed to use a Back-Propagation neural network in image segmentation [26]. The neural network is trained on the set of manually segmented samples. Segmentation is performed pixel by pixel. The inputs to the neural network are the class membership probabilities of the pixels from a neighborhood around the pixel being classified. Therefore, contextual rules can be learned and spatial consistency of the segmentation can be improved.

Classification-based segmentation algorithm requires training. The training parameters are usually set in a trial-and-error manner, which is subjective. The accuracy of this algorithm largely depends on the selected training samples. Also, classification-based segmentation algorithm is more tedious to use.

2.1.6 Deformable Model

Numerous deformable models have been proposed, and the most important ones are discussed below.

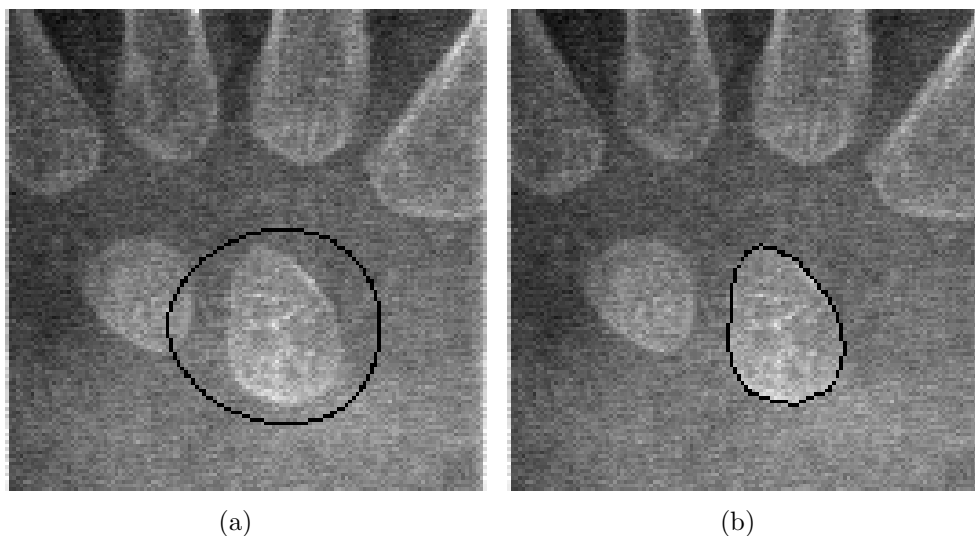


Figure 2.10: Snake segmentation of bone [28]. (a) The initial contour (black curve). (b) Segmentation result (black curve) (from <http://www.cvc.uab.es/~petia/dmcourse.htm>).

A. Active Contour Models (Snake)

The *snake* model was first proposed by Kass *et al.* [27]. It is a controlled continuity spline which can deform to match any shape under the influence of two kinds of forces. The internal spline forces serve to impose a piecewise smoothness constraint. The external forces (image features) attract the snake to the salient image features such as lines, edges and terminations. The snake algorithm iteratively deforms the model and finds the configuration with the minimum total energy, which hopefully corresponds to the best fit of the snake to the object contour in the image (Figure 2.10).

Atkins and Mackiewicz [28] used the active contour for brain segmentation. The input image is first smoothed. Then, an initial mask that determines the brain boundary is obtained by thresholding. Finally, segmentation is performed by the snake model.

Snake is a good model for many applications, including edge detection, shape modeling, segmentation and motion tracking, since it forms a smooth contour that corresponds to the region boundary. However, it has some intrinsic problems. Firstly, the result of the snake algorithm is sensitive to the initial configuration of the snake. Secondly, it cannot converge well to concave parts of the regions.

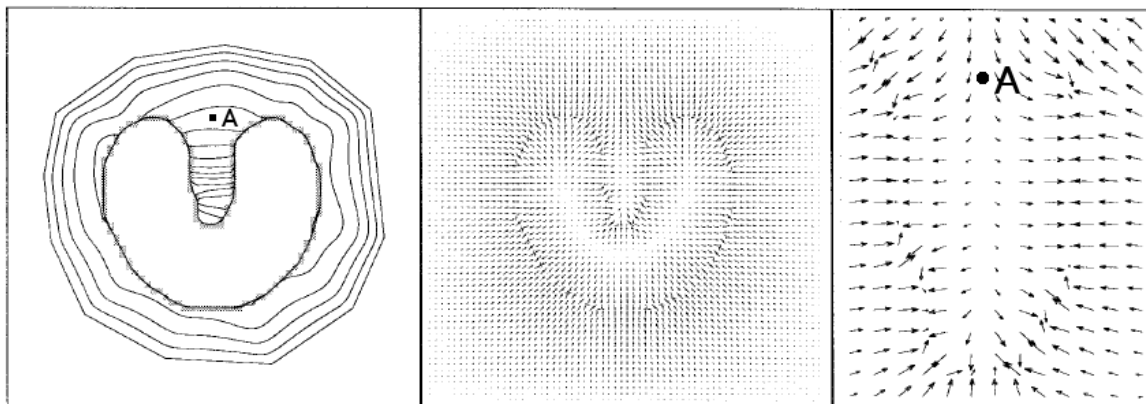


Figure 2.11: Gradient vector flow [29]. Left: deformation of snake with GVF forces. Middle: GVF external forces. Right: close-up within the boundary concavity.

An analysis of the snake model shows that its image force, usually composed of image intensity gradient, exists in a narrow region near the convex part of the object boundary. A snake that falls in a region without image forces cannot be pulled towards the object boundary. Snake with Gradient Vector Flow (GVF), proposed by Xu and Prince [29], partially solved this problem by pre-computing the diffusion of the gradient vectors (gradient vector flow) on the edge map (Figure 2.11). As a result, image forces exist even near concave regions, which can pull the snake toward the desired object boundary. GVF is less sensitive to the initial configuration of the contour than the original snake model. However, it still requires a good initialization and can still be attracted to undesired locations by noise.

B. Level Set

Snake-based deformable model cannot handle evolving object contours that require topological changes. For example, when two evolving contours merge into one contour (Figure 2.12), an algorithm that represents the contours by connected points needs to remove the points inside the merged region. This is computationally expensive, especially for the 3-D case.

Sethian proposed a *level set* [30] approach to solve the above problem by embedding the contour in a higher dimensional surface called the level set function. The contour is

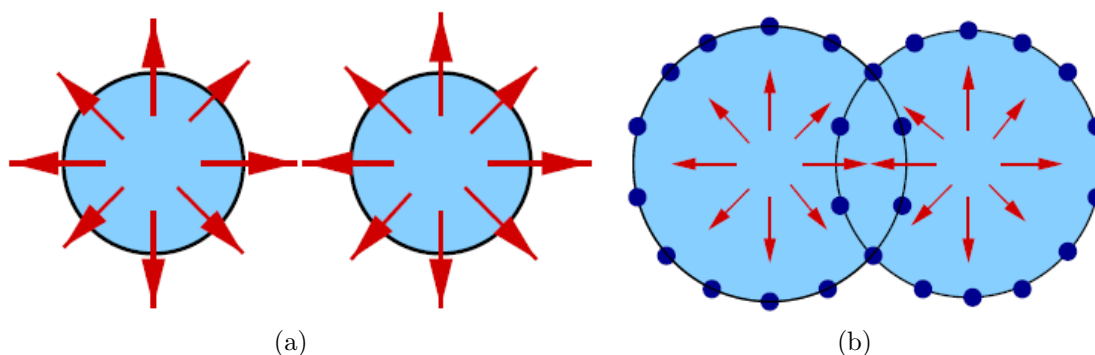


Figure 2.12: Merging of contours [31]. (a) Two initially separate contours. (b) Two contours are merged together.

exactly the intersection between the level set function and the x - y plane, and corresponds to the boundary of the object to be segmented. For 2-D contour, the level set function $z = \phi(x, y, t = 0)$ is represented as a 3-D surface, of which the height is the signed distance from a point (x, y) to the contour in the x - y plane. This constructs an initial configuration of the level set function ϕ . The contour is the zero level set of the level set function, i.e., $\phi(x, y, t = 0) = 0$.

The evolution of the contour is propelled by some force F . F may depend on many factors, such as local geometric information and global properties of the contour. Once the level set function is constructed, the evolution of the interface can be easily computed. The level set function actually represents all possible states of the evolution of the contour, which cannot be constructed in advance. To solve this chicken-and-egg problem, instead of constructing the whole level set function directly, the evolving zero level set is computed iteratively based on the force F .

The iterative algorithm needs to update only the level set function values near the current object boundary. This leads to the narrow band method [30]. If the contour propagates only in one direction, the fast marching algorithm [30] can be used.

The major advantage of the level set approach is that the level set function remains a single function while the zero level set may change topology, break, merge and form sharp corners [32]. However, it generally cannot maintain shape information, and is sensitive to noise.

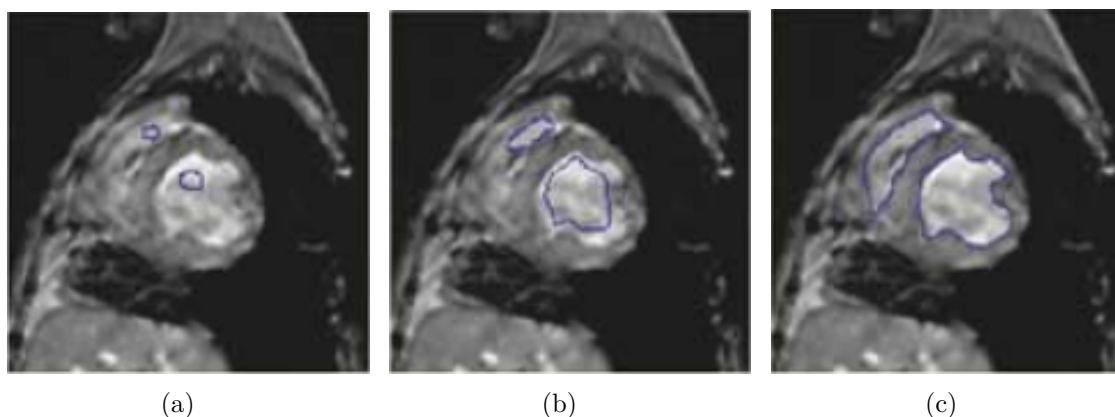


Figure 2.13: Level set segmentation of heart image [34]. (a) Initial contour (blue curve). (b) Evolving contour. (c) Final contour.

Level set is quite popular in the literature of medical image segmentation, and quite a number of improvements have been proposed. To deal with the noise problem, Droske *et al.* proposed to incorporate curvature terms in the velocity function [33]. They also proposed an adaptive grid to speed up the fast marching algorithm. To restrict the evolution of the zero level set, Yang *et al.* proposed a Level Set Distribution model (LSDM) [34], which is similar to the Point Distribution Model described in the next section. The segmentation process is shown in Figure 2.13.

C. Active Shape/Appearance Model

Many objects in medical images, such as organs, cells, and other biological structures, have a tendency towards some average shape. When a collection of shapes of the same organ is available, standard statistical analysis can be applied. The *active shape model* (ASM) [35] and the *active appearance model* (AAM) [36], proposed by Cootes *et al.*, are widely used when a set of training samples are available.

In ASM, a training shape is usually represented by a $2n$ -dimensional vector $(x_1, y_1, x_2, y_2, \dots, x_n, y_n)$ containing coordinates of points on the shape. The shape vector corresponds to a point in a high-dimensional ($2n$ -D) space called the eigen space. Thus, ASM is also known as Point Distribution Model (PDM). Therefore, all the training samples form a point cloud in the eigen space. ASM applies Principal Component Analysis

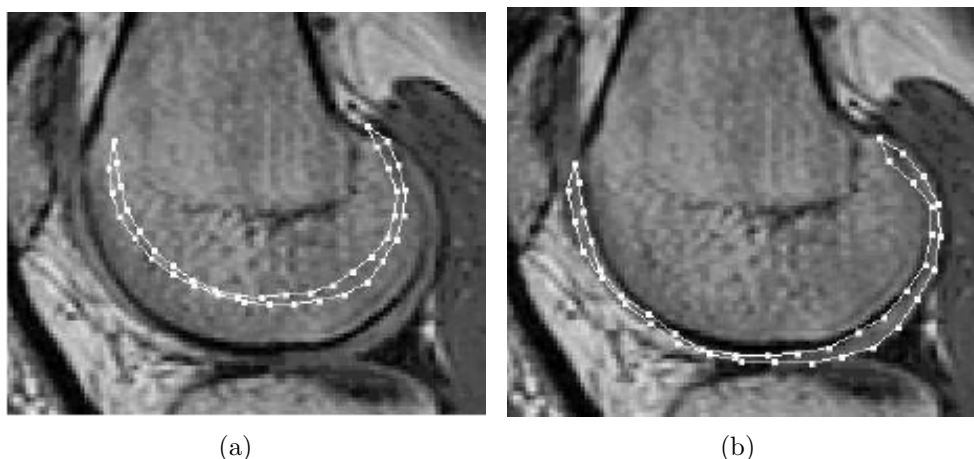


Figure 2.14: Segmentation of cartilage by active shape model [38]. (a) Initial contour (white curve). (b) Resultant contour after 14 iterations.

(PCA) on this point cloud to identify the eigenvectors (eigenshapes) that describe the point cloud. An arbitrary shape can be represented by the linear combination of these eigenshapes with different coefficients. A model can be deformed by changing these coefficients. An initial guess can be randomly generated as proposed by Hill [37]. Then, an optimization algorithm such as genetic algorithm or direct searching in the eigen space can be used to find the optimal solution. Segmentation of cartilage on MR images are shown in Figure 2.14. In comparison, AAM incorporates not only shape information but also gray level information, and improves the robustness of ASM.

Based on Cootes' model, Wang and Staib [39] applied smoothness covariance matrix to make the neighboring points on the shape correlated, i.e. the neighboring points on the shape are more likely to move together. To bias the search process in a certain range, a Bayesian formulation based on prior knowledge is proposed. The prior of shape and pose parameters is modeled as a zero-mean Gaussian distribution. Similar work was done by Gleason *et al.* [40] in detecting kidney disease in CT images.

The advantage of ASM and AAM is that the shape can be deformed in a more controllable way compared to snake and level set method. One of the disadvantages of these algorithms is that they require a lot of training samples to build a point distribution in the high-dimensional eigen space. An eigen space with a small number of eigenshapes may not be able to generate the desired shape, while an eigen space with a large number

of eigenshapes may incur high complexity in finding the optimal solution.

2.1.7 Summary

General medical image segmentation algorithms can be evaluated according to the information used, performance, computational complexity, sensitivity to noise, manual initialization, and training requirement. Thresholding algorithm uses the information based on single pixel and does not take spatial information into account, whereas other algorithms mainly use information based on a local patch or global information. The segmentation result of thresholding algorithm highly depends on the intensity distribution of the images. Edge-based algorithm tend to produce disjoint edges. Region-based algorithms require that the target objects to be segmented have homogeneous features. Thresholding, region-based and graph-based algorithms generally have over-segmentation tendency.

The computational complexities of thresholding, region-based and edge-based algorithms are roughly linear, while those of the other two algorithms are higher, especially for algorithms based on deformable models. Quite a number of numerical algorithms have been proposed to speed up the deformable models, such as narrow band method and fast marching method for level set.

All the algorithms are sensitive to noise, but deformable models include constraints that make them less sensitive to noise. Region-based algorithm and deformable models usually require manual initialization. Classification-based algorithm and active shape and appearance models require training samples.

In general, thresholding, region/edge-based, graph-based and classification-based algorithms can solve simple medical image segmentation problems. The target image is usually noise free and of high contrast, and features of the target structures are quite homogeneous. For complex medical image segmentation problems, deformable models have more potentials.

2.2 Atlas-based Segmentation Methods

An atlas is a model that contains domain information of anatomical parts. In practice, an atlas is usually obtained by manually segmenting and labeling one or a set of n -dimensional images containing the same anatomical parts. The basic idea of atlas-based segmentation is to register the atlas to the input images and label the input images according to the atlas.

Broadly speaking, existing methods use either a non-probabilistic atlas [41, 42, 43, 44, 45, 46, 47, 48, 49, 50, 51, 52, 53, 54, 55, 56, 57, 58, 59, 60] or a probabilistic atlas [16, 61, 62, 63, 64, 65, 66, 67]. In the probabilistic case, the probability of a voxel belonging to certain tissue type [16, 64] or probabilistic shape in active shape model are used. The representations of probability are often Gaussian [16, 64].

Atlas-based segmentation methods consist of two major stages, namely *global alignment* and *local refinement*. These two stages are discussed in more detail in the following sections.

2.2.1 Global Alignment

The purpose of global alignment is to align the position, scale and rotation of the atlas to the input image. “Global” means that each part of the atlas undergoes exactly the same transformation, which includes scaling, rotation and translation.

Several transformation types, such as similarity transformation and affine transformation, are frequently applied. Affine transformation [42, 46, 47, 49, 50, 53, 54, 60, 62, 63] has the highest Degrees of Freedom (DoF). It captures rotation, scaling, translation and shearing. Similarity transformation [44, 48, 52, 68] includes rotation, scaling and translation. These transformations are all linear transformations and have very low computational complexity. Non-linear transformations (usually low-order polynomial) may also be used [50], since they can capture more variation of the atlas, thus making the global alignment more accurate. At the same time, their computational complexity is relatively low. Rigid transformation is seldom used since it only captures rotation and translation.

The transformation can be performed either manually or automatically. Semi-automatic

methods are also proposed. Gansor *et al.* applied a manual approach which manipulates a grid to match the atlas and input images [51]. Semi-automatic schemes normally include a common procedure, which is manually selecting landmark points, and thus, establishing correspondence between the atlas and the input images. The rest of this section reviews the automatic methods.

Aboutanos *et al.* [41] applied morphological operations to segment the surface of brains. Their algorithm erodes an initial model with a 2-D circular disk, which has 11 pixels in diameter. The algorithm is claimed to guarantee the placement of the model inside the cortical area. However, this algorithm assumes that the organ in the atlas and in the target image are very similar in position. It is very specific and cannot be easily generalized. Especially when the initial model and the organ in the target image are quite different, this algorithm will fail inevitably.

For the rest of the automatic methods, we further classify them into two groups. One group actively searches for correspondence, and the other group does not search for correspondence explicitly.

Iterative Closest Point (ICP) and optical flow-based algorithms belong to the first group. When performing registration, for each (sampled) point on the atlas, ICP iteratively searches for the nearest point on the target as a possible correspondence, solves a transformation matrix, and updates, i.e., transforms the atlas, until the sum-squared difference between the atlas and the target is minimized. ICP can be regarded as a geometric method. Optical flow-based algorithm, on the other hand, is a photometric method. It borrows the idea from tracking, and treats the atlas and target image as neighboring frames in a temporal motion sequence. In each iteration, the algorithm uses optical flow to search for the correspondence between the atlas image and the target image, and computes the displacement of each point in the image. A Gaussian filtering step is often applied to smooth the displacements.

Optimization-based algorithms belong to the second group. The main framework of optimization-based algorithms is to formulate a similarity or dissimilarity function between the atlas and the target, and apply optimization algorithm to maximize or minimize that function. The similarity or dissimilarity functions proposed can be sum of squared differences between the intensities of corresponding voxels [44, 60, 68], chamfer



Figure 2.15: Iterative corresponding point [49]. The white contours iteratively converge to the actual boundary of the soft tissues. In each iteration, the algorithm searches for corresponding points with most similar features.

distance [46, 47], correlation ratio [42, 54], or mutual information [48, 50, 52, 53, 62, 63]. The optimization algorithms applied include gradient descent, Levenberg-Marquardt, simulated annealing, etc.

2.2.2 Local Refinement

The purpose of the local refinement is to align the atlas and the target as accurately as possible. “Local” means that different parts of the atlas may undergo different transformations. Since accuracy is the main objective, the methods used in this stage have to focus on the details of the atlas and the target image. Therefore, they are highly complex. Local deformation and pixel classification are two major approaches used for the local refinement stage.

A. Local Deformation

Local deformation deforms the atlas locally and fits it to the target image accurately. A number of methods have been proposed to solve the local deformation problem. Some methods actively search for or guess the corresponding points in the target image. Thirion [69] named such methods as attraction models, since the model is attracted by image features and deformed to match the target image.

Ding *et al.* proposed an Iterative Corresponding Point algorithm [49], which belongs to the attraction model. The proposed method is similar to the original ICP. Apart from that, it uses intensity difference distribution (IDD) along the contour to find possible correspondence. It computes IDD of each point along the contours in the atlas, and searches for corresponding point in a small neighborhood in the target image that has the most similar IDD. Once the correspondence is established, an affine transformation matrix is computed to transform the atlas contours. The process discussed above is repeated until convergence (Figure 2.15). Finally, the GVF snake is applied to extract accurate object boundaries.

Diffusion-based algorithms such as demons algorithm [69] is very popular, and it is used in [16, 42, 44, 46, 47, 48, 52, 68]. In the demons algorithm, the deformable model or image diffuses through the fixed target image by the action of the effectors called demons located on the object boundaries in the target image. Demons act locally to pull the deformable models towards the target image.

Figure 2.16 shows a comparison between the attraction method and the diffusion method during a registration process. For the attraction method, the points located on the model contour are attracted by the closest points on the target contour. On the other hand, for the diffusion method, the model is pulled into the target by the action of the demons located on the target contour.

Demons algorithm has several variations based on the selection of the demons' positions, the types of deformations, and the forces of the demons. In the most popular variation, all pixels in the target image are selected as the demons. For each demon, a displacement is computed by the optical flow algorithm. A Gaussian filter is then applied to obtain a smooth displacement field. The above process is iterated until the final displacement field is obtained, which represents the deformation of the model.

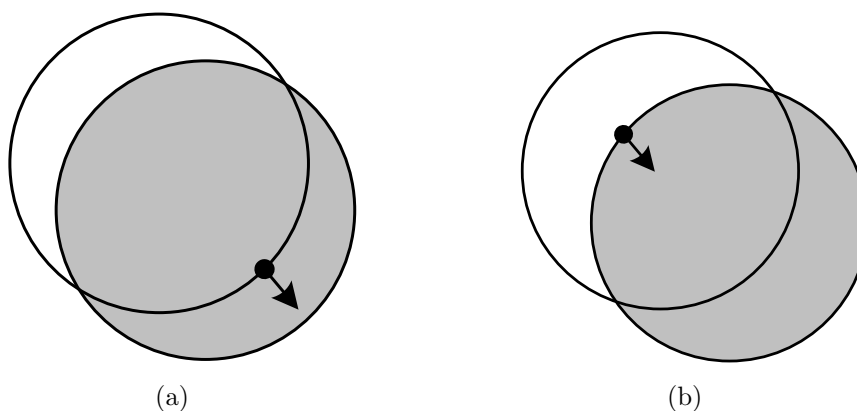


Figure 2.16: Attraction vs. diffusion methods. The model is represented by a white disk, and the target by a gray disk. (a) In the attraction method, the point (black dot) on the model contour is attracted by the closest point on the target contour. (b) In the diffusion method, the demon (black dot) on the target contour pulls the model towards itself.

PASHA [70] proposed by Cachier *et al.* is used in [54]. PASHA algorithm incorporates both geometric features and intensity features. The energy function of PASHA contains three components: intensity similarity, geometric distance, and a regularization term. The intensity similarity term measures the local correlation between the points in the source image and those in the target image. The geometric distance measures the disagreement between the estimated point correspondence and the computed deformation. The regularization term imposes smoothness constraints. A gradient descent algorithm is used to optimize the energy function and, in the process, estimate the point correspondence, and compute the deformation. Large displacement vectors are not favored. A comparison between the results of demons algorithm and PASHA is shown in Figure 2.17. The displacement field produced by PASHA is smoother than that produced by the demons algorithm.

Some local deformation methods are based on the standard optimization algorithm. Aboutanos *et al.* [41] proposed a cost function that combines intensity, morphology, gradient, deviation from previous contour and smoothness. They used an optimization algorithm to minimize the cost function and transform the initial contour to fit the brain.

Standard deformable models are also used in the local refinement stage such as snake and its modified versions [49, 56, 61], level set [50, 60]. For example, Ding *et al.* [49]

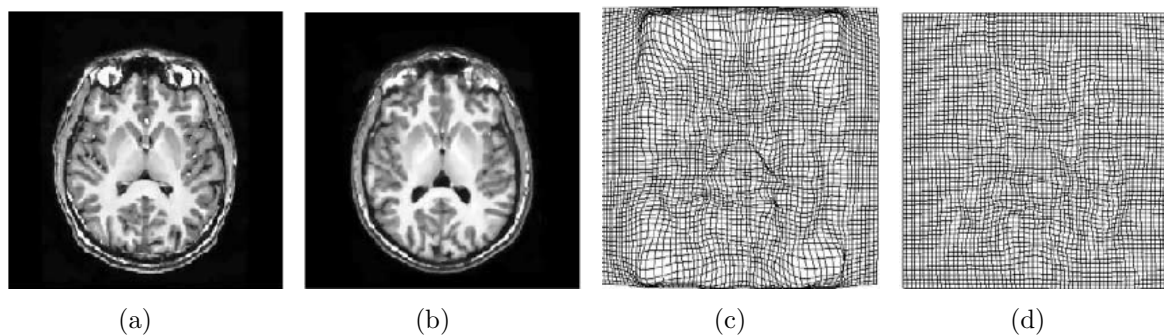


Figure 2.17: PASHA vs. demons algorithm [54]. (a) Deformable template. (b) Fixed target image. (c) Displacement field produced by demons algorithm on a grid. (d) Displacement field produced by PASHA on a grid. The results suggest that the displacement field produced by PASHA is smoother than that produced by the demons algorithm.

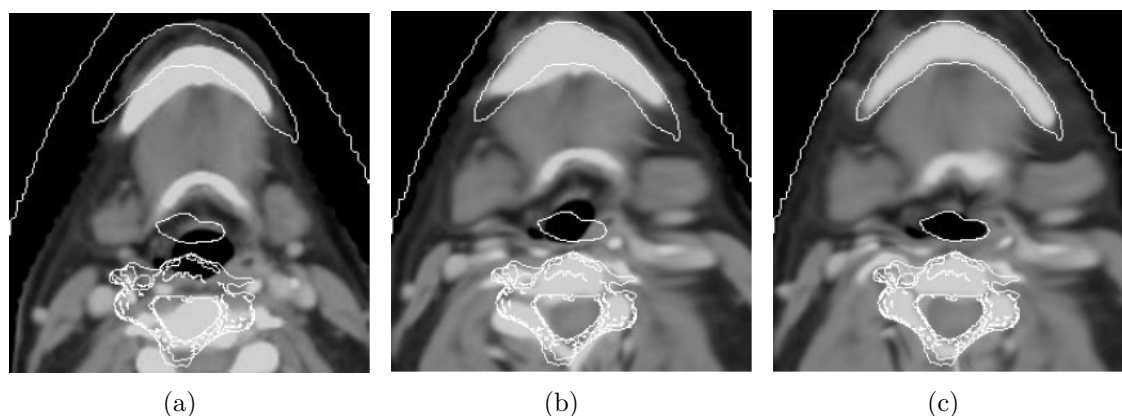


Figure 2.18: Level set algorithm applied to neck axial slice [50]. (a) Initial contour (white curves). (b) Intermediate deformation step. (c) Segmentation result.

applied snake with GVF algorithm for final contour refinement. Duay *et al.* [50] applied level set algorithm to perform local deformation after global alignment (Figure 2.18).

B. Pixel Classification

Pixel classification method separates the pixels into several groups, and each corresponds to an anatomical part. It is usually performed in probabilistic atlas-based segmentation. Classification is based on maximizing a posterior probability of a pixel belonging to a particular anatomical part. The features used in pixel classification is usually intensity

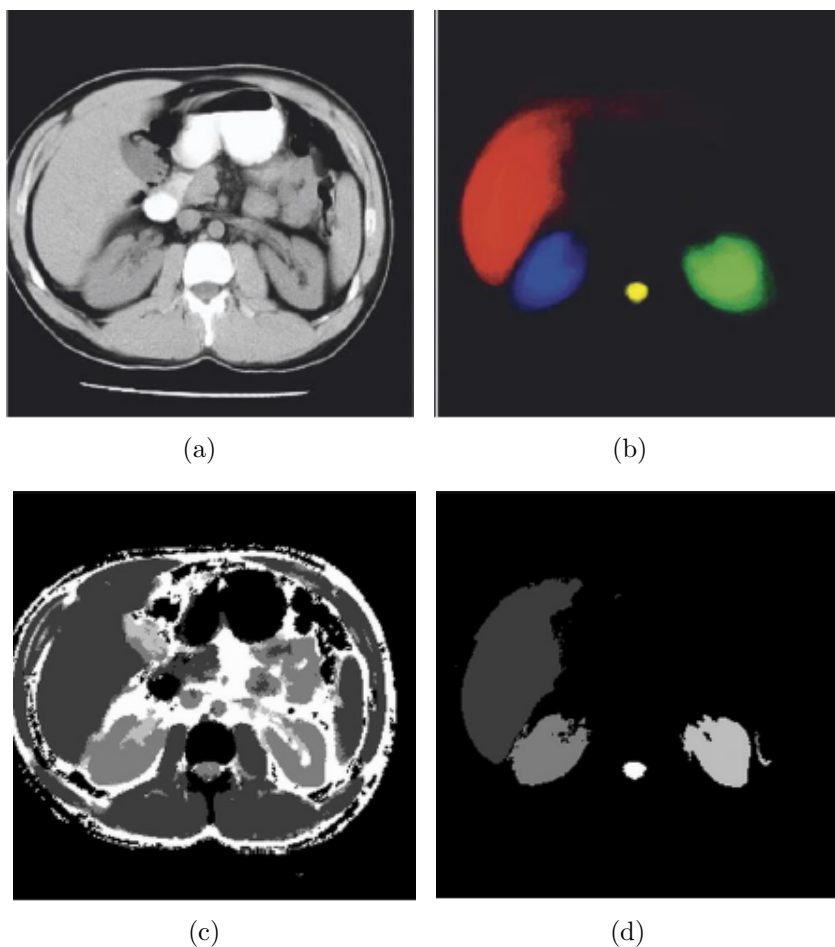


Figure 2.19: Pixel classification [64]. (a) One slice of CT image. (b) Atlas information. (c) Segmentation result without atlas information. (d) Segmentation result with atlas information.

and position information of the pixel. Park *et al.* [64] proposed to classify pixels using a Bayesian framework. Pixels are classified into 5 groups: liver, right kidney, left kidney, spinal cord and “none of the above”. The atlas is constructed from manually segmented organs from 32 registered CT slices. The intensity value of each pixel in the atlas image corresponds to the probability that it belongs to certain organ. The cost function to be maximized contains a Maximum A Posteriori (MAP) formulation that estimates the classes of the pixels that best explain the given input image. It also includes a Markov Random Field (MRF) regularization term, which penalizes dissimilar adjacent labels (Figure 2.19).

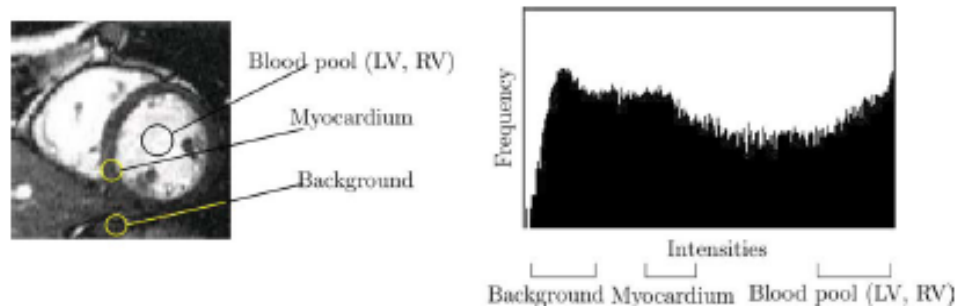


Figure 2.20: Heart intensity distribution [63]. A heart MR image showing sample regions of the blood pool of the left ventricle (LV), right ventricle (RV), myocardium, and the corresponding histogram of the intensity distribution of the image.

Lorenzo *et al.* [53, 62, 63] proposed a classification algorithm to segment heart images. The intensity distribution of each class that corresponds to an organ is modeled by a Gaussian distribution. The mean and variance of the distribution are computed by Expectation Maximization (EM) algorithm based on the training samples. Figure 2.20 shows an example intensity distribution corresponding to different tissues in a heart MR image. The classification is also followed by a MRF regularization process similar to [64].

Prastawa *et al.* [65] used Minimum Covariance Determinants (MCD) [71] to generate robust mean and variance of unimodal intensity distribution, and then classified pixels in a Bayesian framework. The MCD estimator computes the mean and covariance that have the smallest determinant of covariance.

2.2.3 Summary

Atlas-based segmentation algorithms often consist of two major stages, global alignment and local refinement. In the global alignment stage, the atlas is transformed to roughly align with the input image. In the local refinement stage, different parts of the atlas may undergo different refinement. Attraction-based algorithms can easily transform the model even if the distance between the model and the target is large. But it may be trapped in local minimum if the initial configuration is not good. Diffusion-based algorithms such as demons and its variations usually cannot perform well when the displacement between the model and the target is large. The standard method for solving this problem is to

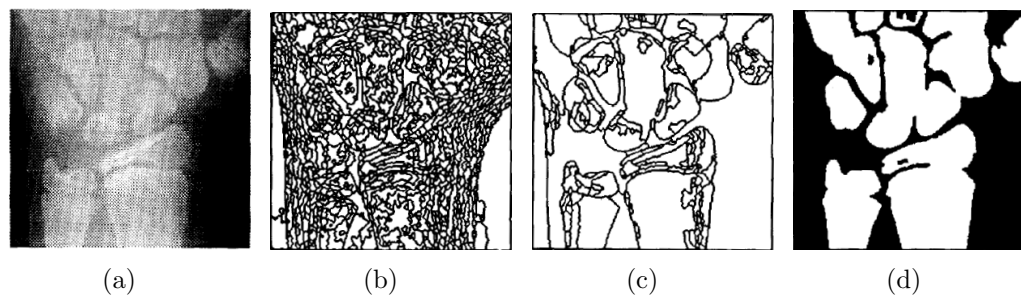


Figure 2.21: Region-based wrist x-ray image segmentation [72]. (a) Input image. (b) Result obtained by region growing. (c) Result obtained by region merging. (d) Final result.

apply the algorithm in an image pyramid.

Snake model is good in the sense that it is a connected contour and is quite flexible for representing a region boundary. However, it is sensitive to noise in the image and its initial configuration. Moreover, its parameters need to be set in a trial-and-error manner. Level set has the ability to handle topology changes of contours, and efficient numerical algorithms have been proposed. However, it is sensitive to image noise. Pixel classification can utilize domain knowledge encapsulated in the probability distribution, but it requires training. The features used are usually intensity and position of the pixel, which are not so reliable in the x-ray images. Moreover, the boundaries of the target organs produced by pixel classification are usually not precise.

Atlas-based segmentation methods use prior knowledge to guide the segmentation process. It is ideal for segmenting complex medical images, which cannot be handled robustly by general segmentation methods.

2.3 Segmentation of X-ray Images

In comparison to the segmentation of images in other modalities, less research has been performed on the segmentation of ordinary x-ray images. Existing algorithms for the segmentation of x-ray images often rely on some general medical image segmentation methods.



Figure 2.22: Thresholding based on fuzzy index measure [73]. The white part is bone, the gray part is skin and the black part is background. The region of bones are disjoint.

2.3.1 Region-based

Manos *et al.* applied a region-based algorithm [72] to segment hand and wrist bones. The algorithm starts with a region growing stage. Region growing will produce an over-segmented image (Figure 2.21(b)). This is followed by a region merging stage, which incorporates region similarity, size, connectivity and edge information (Figure 2.21(c)). The final segmentation result (Figure 2.21(d)) is obtained by region labeling according to some heuristic rules based on gray-level information.

2.3.2 Classification-based

El-Feghi *et al.* [73] applied a fuzzy set algorithm to segment lateral skull images. Three crisp subsets, namely background, skin and bones are determined by minimizing a fuzzy index function. The fuzzy index function decreases as the similarity between two pixels increases. As no spatial information is considered, the segmented bone regions are disjoint (Figure 2.22).

McNitt-Gray *et al.* [74] proposed to segment chest radiographs into anatomical regions using neural networks. 59 features including the gray level information, local difference measures and local texture measures are used as the input of the neural network. Spatial information is also used to correct mis-classified pixels.

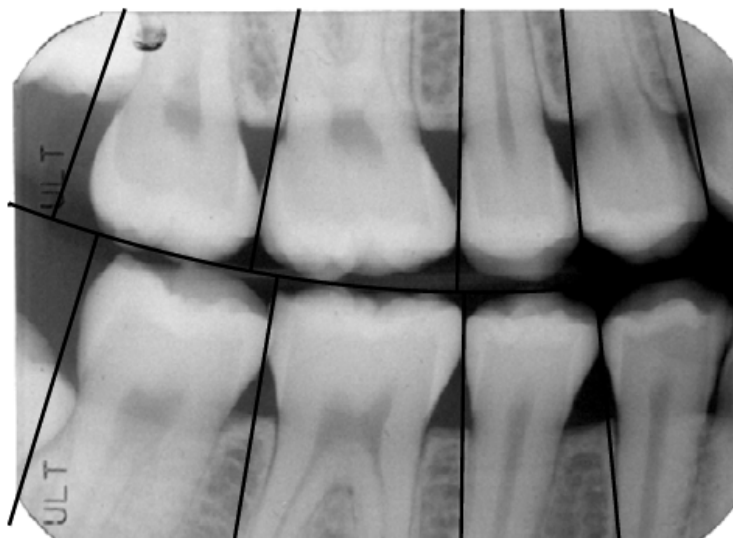


Figure 2.23: Initialization of tooth contour extraction [78].

Classification-based algorithms are generally not effective for x-ray image segmentation due to the intrinsic properties of x-ray images, i.e., images of different body parts overlap.

2.3.3 Deformable Model

Most of the x-ray image segmentation work is based on deformable models, especially active contour model. In order to locate the rib border in chest radiographs, Yue *et al.* [75] first determined the thoracic cage boundary to restrict the search space. Hough transform was then used to find approximate rib borders. The snake model was finally applied to refine the rib borders.

Jiang *et al.* used geodesic active contour [76] to segment forearm bones [77]. Geodesic active contour is based on the traditional snake model, and evolves over time according to geometric measures (curvatures) of the image. The initial snake contour is manually segmented from the x-ray image of the patient at the initial visit to the hospital.

Chen and Jain [78] applied snake model to extract the contours of teeth. To get the initial configuration of the snake model, they detected the gap between upper and lower teeth and the gap between neighboring teeth (Figure 2.23).

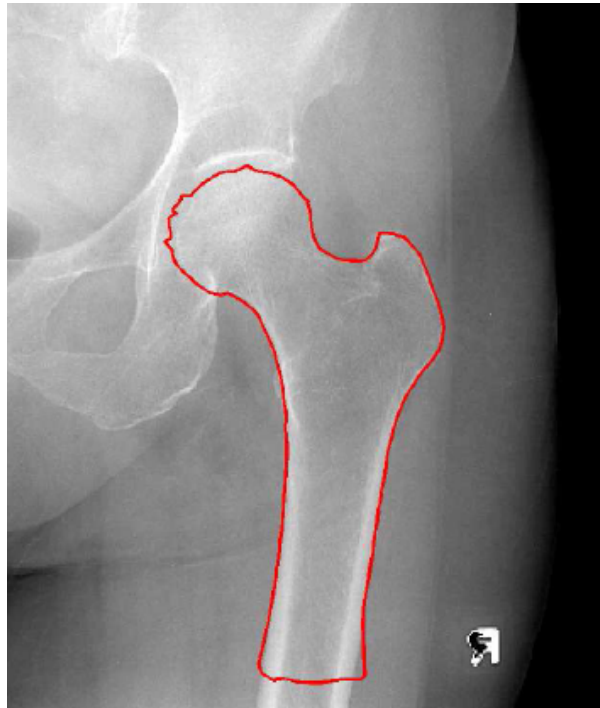


Figure 2.24: Segmentation result of femur [79].

Chen *et al.* proposed an incremental approach to segment femur bones [79] (Figure 2.24). Salient features in the x-ray images including parallel lines in the shaft area, circles in the femoral heads are first detected. Then, a 2-D femur model is fitted onto the input x-ray images to match the features. The final femur contours are refined by a snake algorithm with curvature constraints. To achieve this, a spring force which describes the difference between the actual curvature of the snake and the reference curvature of the model is introduced. Chen's work only considered femur bones in the x-ray image without exploiting the spatial relationship between pelvis and femur bones.

Similar work (femur segmentation) has been done by Behiels *et al.* [80]. The proposed algorithm is based on active shape model. The major contribution is that a regularization term representing the smoothness of shape change in each iteration is incorporated.

In [81], Ballerini and Bocchi added an internal energy term to the snake framework to model the spatial relationships between adjacent bones to segment the hand bones. This energy term is represented by an elastic force that connects appropriate points of adjacent snakes. The snake model is represented in polar coordinates. The polar representation

has the advantage that it introduces ordering of the contour points and prevents the snake elements from crossing each other during evolution. However, it may run into problem when representing a concave shape. In snake optimization stage, the snake configuration is coded into chromosomes, and genetic algorithm (GA) is applied to minimize the energy of the snake. This may alleviate the sensitivity to the initial contour placement, which is chosen randomly.

A semi-automatic approach was proposed by Bernard *et al.* [82], which incorporated an articulated model to segment the cervical spine. Articulated structures normally exhibit two kinds of shape variations, i.e., variations in shapes of individual parts and variations in spatial relationships between the parts. A hierarchical PCA was proposed to deal with this problem. The hierarchical PCA consists of a topological PCA describing topological variations of an articulated structure, i.e., the spatial organization of anatomical structures, and a shape PCA describing the shape and pose variations of individual structures.

2.3.4 Geometric Model

In [83], Vinhais and Campilho created a geometrical model of lungs (Figure 2.25) by computing a mean shape from the training images. They applied a Laplacian of Gaussian (LoG) filter with high standard deviation on the image to extract some anatomical landmarks (Figure 2.26(a)) for an initial rough registration. They used genetic algorithm (GA) to find the coefficients of the geometric model in the free-form deformation stage. Each chromosome of GA contains an ordered list of the control points of a free-form deformation grid [84]. Segmentation result is shown in Figure 2.26(c).

The major problem of this algorithm is that the anatomical landmarks may not be reliably extracted because LoG filter is easily affected by noise. This will cause the free-form deformation to fail. Moreover, GA usually takes a large amount of computation time to produce a reasonable solution.

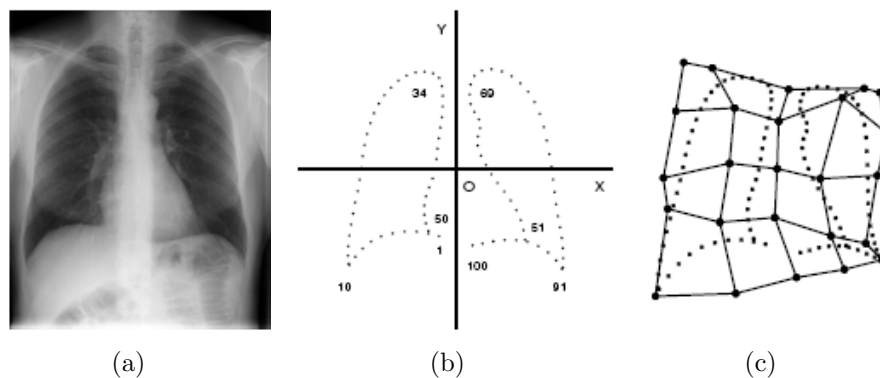


Figure 2.25: Geometrical model [83]. (a) Chest x-ray image. (b) Geometrical model. (c) Deformation of (b) using free-form deformation grid.

2.3.5 Atlas-based Method

Boukala *et al.* [85] applied atlas-based segmentation method to segment pelvis and femur images. First, an atlas is built from a set of 24 manually landmarked training images. The landmarks consist of 20 easily located anatomical features along the boundary of the bones (Figure 2.27(a)). To increase the number of points, boundaries between these landmarks are subdivided regularly. The femurs are rotated around the femoral head center to make all the angles in different training images the same (Figure 2.27(b)). Next, corresponding points between the training images are obtained. Active shape models are constructed based on these corresponding points for the femurs and the pelvis separately.

In the global alignment stage, the pelvis and the femur are registered independently. The average model shape is first registered to the input image. To do this, the shape context descriptor [86] is used to find the correspondence between the points on the model contour and those on the edges in the input image. For each point on both the model contour and the edges in the image, the shape context computes the distribution of neighboring points located in a log-polar coordinate system (Figure 2.28). This gives a histogram-like descriptor for each point. For each model point, correspondence is found by searching for the edge point with the most similar shape context descriptor. Due to the presence of noise in the image, shape context method is not robust enough to find the correct correspondence.

In the local refinement stage, active shape model is used to search for the boundaries

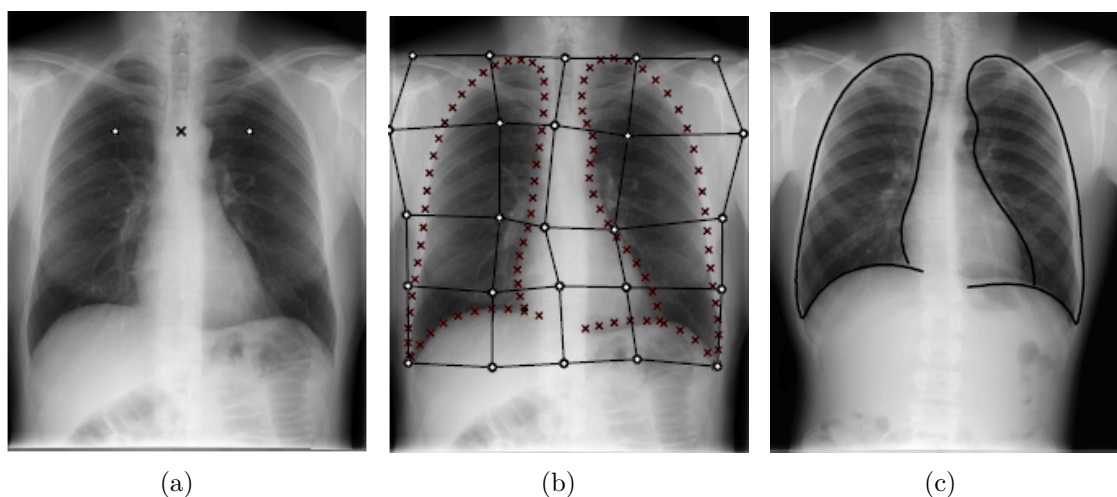


Figure 2.26: Geometric model-based lung segmentation [83]. (a) Extracted landmarks. (b) Displaced grid and corresponding deformed model. (c) Segmentation result.

of the bones. The boundaries of the femurs and the pelvis are extracted independently using different active shape models (ASM). The shortcoming of ASM is that the extracted boundaries may not be accurate because a large number of sample points is required to represent a complex shape. As shown in Figure 3.2, the pelvis has a very complex shape. Although articulations are used in constructing the atlas, they are not employed explicitly in the segmentation process. The segmentation results of this algorithm are not clearly presented in [85].

2.3.6 Summary

The computational complexities of region-based and classification-based segmentation algorithms for x-ray images are low. However, region-based algorithms are easily affected by noise. They are prone to over-segment the images. Classification-based algorithms are not suitable for segmenting x-ray images because images of different tissues may overlap. The other algorithms are more promising for x-ray image segmentation.

Among the existing methods for segmenting x-ray images, those presented in [79, 80, 83, 85] are most related to the proposed research topic. [79] and [80] focus on the segmentation of a single femur bone. Chen *et al.* [79] use domain knowledge of the femur, such as the width of the shaft and the radius of the femoral head, to aid in the

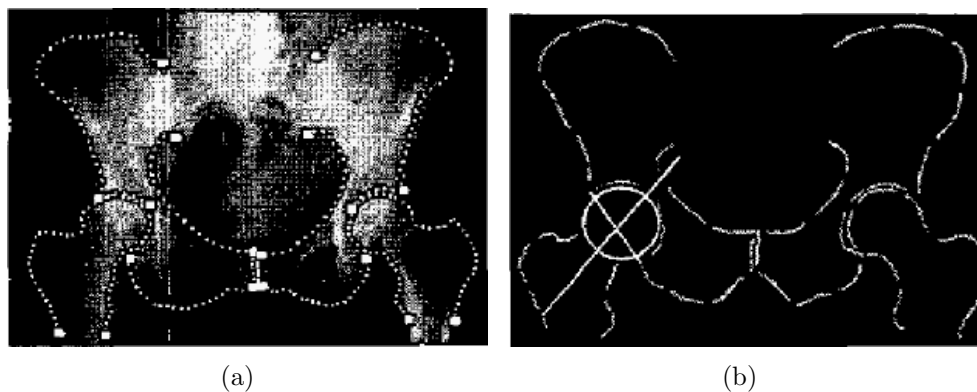


Figure 2.27: Active shape model-based segmentation of hip images [85]. (a) 20 expert-labeled landmarks. (b) The femur is rotated around the femoral head center to adjust the angle between the drawn lines.

segmentation. Behiels *et al.* [80] apply the snake algorithm to segment femur bones.

In [83], genetic algorithm (GA) is used to obtain an optimal deformation of the free-form grid, but it has a high computational complexity. The anatomical landmarks used to initialize GA are extracted by LoG filter. But, LoG filter is not immune to noise. Therefore, the anatomical landmarks obtained using this method may not be reliable.

In [85], segmentation of pelvis and femurs is performed using atlas-based method. Articulation is used in atlas construction to remove the difference in the orientations of the femurs in different images. But, it is not used directly in the segmentation algorithm. Shape context descriptors are used to search for correspondence between the points on the atlas contour and the edge points in the input image. Shape descriptor is affected by noise in the image, which incurs error in global alignment. Active shape models are used in the local refinement stage to extract the boundaries of the femurs and the pelvis separately. As discussed in the previous section, the boundaries extracted may not be accurate.

In conclusion, the problem of segmentation of bone structures in x-ray images is not well studied, and there is a lot of room for significant improvements.

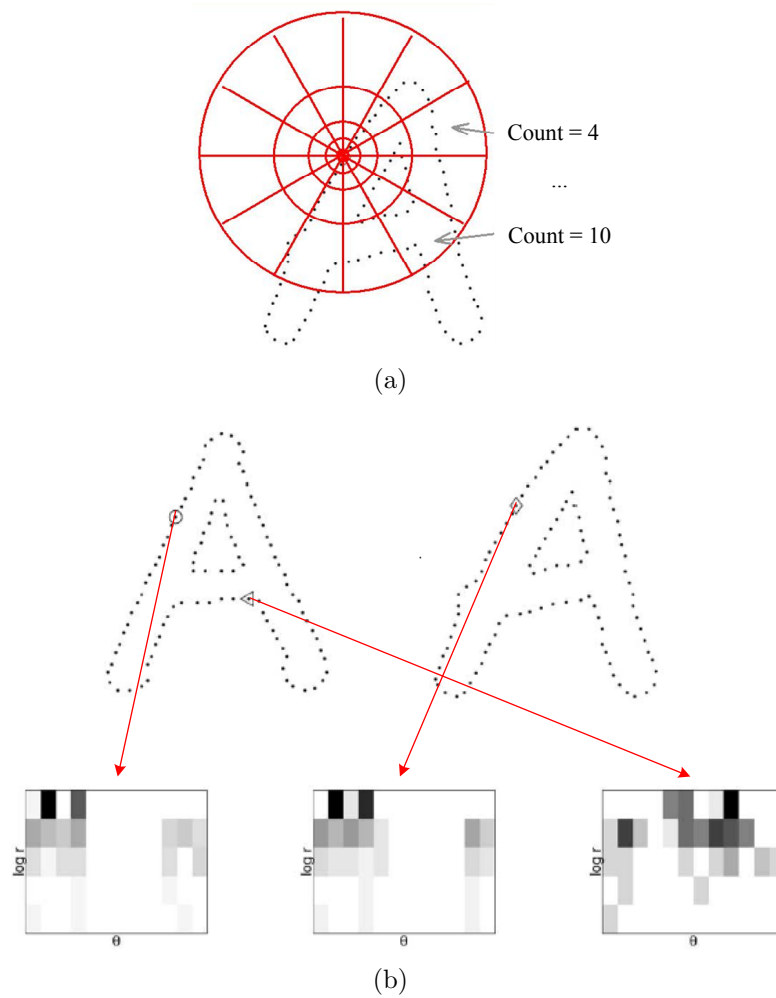


Figure 2.28: Shape context. (a) Log-polar histogram of point distribution counts the number of points inside each bin. (b) Shape context descriptor (from http://www.eecs.berkeley.edu/Research/Projects/CS/vision/shape/sc_digits.html).

Chapter 3

Proposed Research Topic

Segmentation of bones in x-ray images is an important step in medical diagnosis, surgery, and treatment. The review in Chapter 2 shows that this problem has not been well studied. Algorithms for segmentation of a single bone in x-ray images may not be robust enough, and the quantitative segmentation results are seldom reported. This leads to the proposed research topic: segmentation of bone structures in x-ray images.

3.1 Problem Analysis

In order to study the problem of bone segmentation in x-ray images, some characteristics of this problem are analyzed.

- Unlike other medical imaging modalities, bone regions in x-ray images often overlap with other organs, such as flesh, soft tissues and other bones (Figure 3.1). Pelvis region in x-ray images can also be “corrupted” by gas inside the ascending and descending colons or bowel (Figure 3.1).
- Bones are connected with other bones by joints. When the entire bone structure is being segmented, articulation of the bones needs to be considered.
- Bones are 3-D in nature. A simple 2-D closed curve may not be accurate enough to represent the boundaries of bones in x-ray images. For example, the pelvis bone may need to be represented by its outer boundaries as well as inner contours (Figure 3.2).

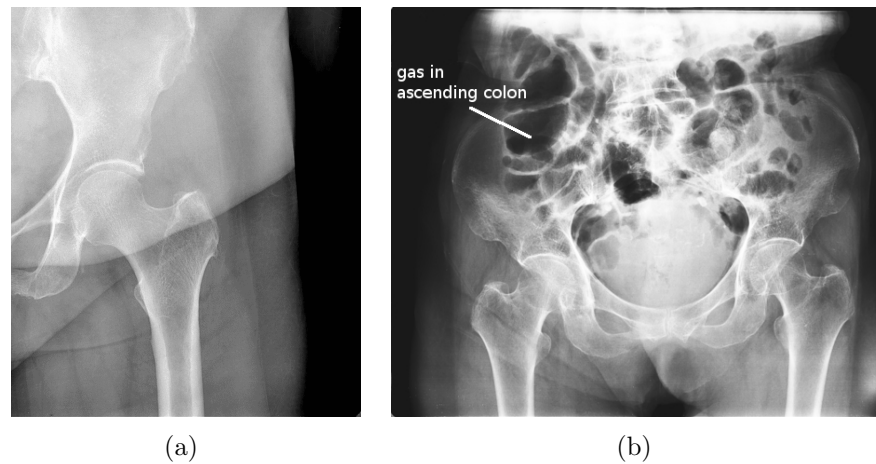


Figure 3.1: Characteristics of x-ray images. (a) Bone regions in x-ray images often overlap with other organs, such as flesh, soft tissues and other bones. (b) Pelvis region is corrupted by gas in the ascending and descending colons.

Segmentation of bone structures in x-ray images is both intrinsically and extrinsically difficult. Intrinsic difficulties refer to those caused by the intrinsic properties of x-ray imaging systems:

- Noise. Noise in x-ray images has a number of origins, but the most fundamental is from the x-ray source itself. This type of noise is called “quantum noise”, in reference to the discrete nature of the x-ray photons producing it (<http://www.lxi.leeds.ac.uk/learning/iq/noise/>).
- Overlapping. As discussed in the characteristics of the problem.

Extrinsic difficulties are usually due to the patients:

- Ambiguity. Neighboring tissues inside human body may have similar x-ray absorption rates. As a result, the boundaries of the organs may be ambiguous. That is, in the image, there is sometimes no clear edge between two neighboring organs.
- Bone density variability. Different patients may have different bone densities, which result in significantly different intensities in the bone regions between their x-ray images. A normal patient usually has dense bones and the x-ray image of bones are bright, whereas a patient who suffers from osteoporosis has low-density bones,

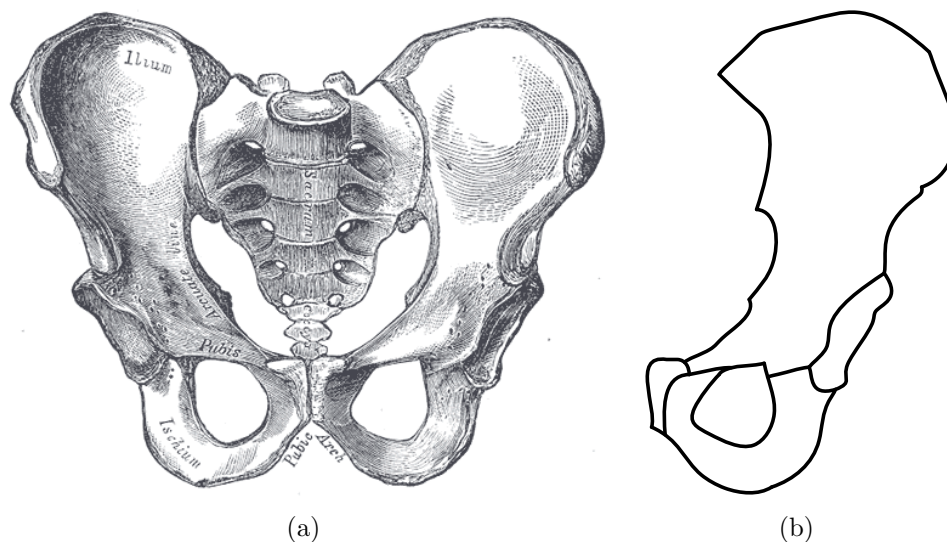


Figure 3.2: Representation of the pelvis bone. (a) 3-D pelvis bone (from <http://www.bartleby.com/107/illus241.html>). (b) 2-D contour representation of the left pelvis bone.

which results in much darker bone images. Moreover, other body tissues may also affect the intensities of bone images.

- Inter-patient shape variability. The shapes of the bones of different patients can differ quite significantly. In particular, the shape of the pelvis bone of a female patient is quite different from that of a male patient. This is due to the fact that females usually have much wider pelvis bones (Figure 3.3).
- Imaging pose variability. The bones may be located in different parts of different images due to different imaging pose (Figure 3.3).

3.2 Problem Formulation

The problem of automatic segmentation of bone structures in x-ray image can be formulated as non-rigid registration of the atlas to the target x-ray image.

- The inputs of the problem:

Let $M = \{m_i\}$ represent the whole reference bone structure in the atlas, $m_i =$

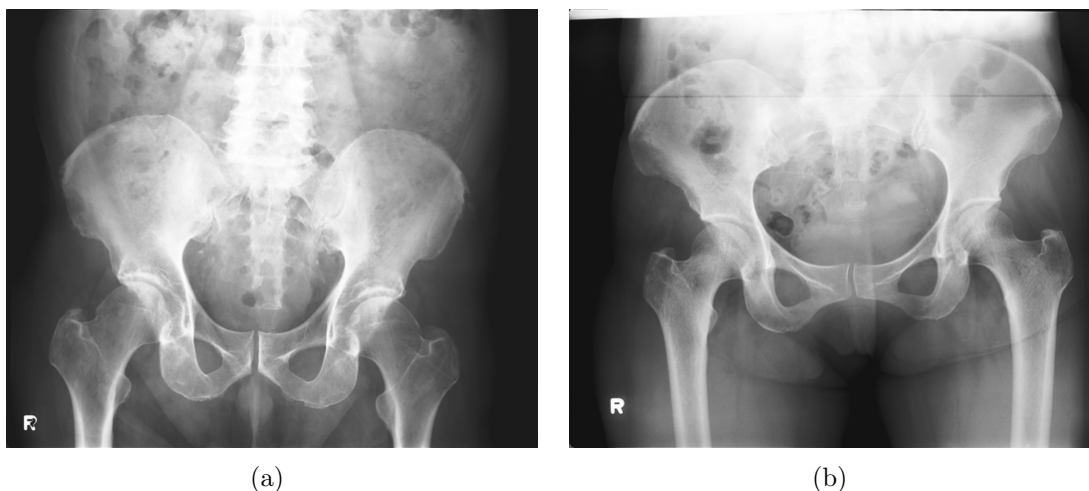


Figure 3.3: Sample pelvis x-ray images. The shape of the pelvis of (a) a male patient differs from that of (b) a female patient mainly because the female has a wider pelvis than the male.

$\{p_{ij}\}$ represent the individual bones in the whole structure connected by joints, p_{ij} represent the control points located on bone m_i . 2-D joint angle between bone m_u and bone m_v is represented by ω_{uv} . S is the shape (e.g., curvature) information of p_{ij} . $C = \{q_j\}$ denotes the set of edge points in the image, which include edge points along the contour of the bones and other noise points, such as edge points along the contours of other body tissues and noise edges, etc. Some points on the contour of the bone structure may not be in C because they are not prominent edge points in the image.

- The output of the problem:

$M' = \{m'_i\}$ is the extracted contour of bone structure in the target image, which is represented by a deformed version of M . $m'_i = \{p'_{ij}\}$ represents the control points on the deformed contours.

We assume that the input x-ray images always contain the full frontal view of the pelvis. The imaging positions for different patients may be different, but the femur bones are shown in the input images.

Let T denote similarity transformation, A denote articulation that can rotate m_u with respect to the joint connected to m_v , D denote a deformation function that can move p_i

to a new position, and f denote a correspondence function from M to C . The aim is to find T , A , D and f such that the total error E is minimized:

$$E = (1 - \alpha) \sum_{p_i} \|D(A(T(p_i))) - f(p_i)\|^2 + \alpha \sum_{p_i} \|S(D(A(T(p_i)))) - S(p_i)\|^2 \quad (3.2.1)$$

where $\alpha \in [0, 1]$ is a parameter. The error E balances the registration error E_p and shape difference E_s to ensure that the deformation D does not severely distort the shape of the bones:

$$E_p = \sum_i \|D(A(T(p_i))) - f(p_i)\|^2 \quad (3.2.2)$$

$$E_s = \sum_i \|S(D(A(T(p_i)))) - S(p_i)\|^2 \quad (3.2.3)$$

3.3 Research Plan

The complex problem of segmenting bone structures in x-ray images can be decomposed into several sub-problems as follows.

1. **Feature Selection** In this step, stable features should be selected to obtain correct correspondence between the points in the atlas and the points in the target image. This is an important first step that will affect the result of the following steps.
2. **Global Alignment** Based on the features found in the above step, global alignment is to determine a rough alignment between the atlas and the image in terms of scaling, rotation and translation. This step is performed with respect to the whole bone structure. In addition, articulations between connected bones should be taken into account.
3. **Local Refinement** Local refinement is to accurately register the atlas contours to the boundaries of the bones. It needs to take into account the articulation and shapes of the bones.

The research plan is to solve each of these sub-problems and then integrate the algorithms into a complete solution.

Chapter 4

Preliminary Work

Two pieces of related preliminary work have been done, i.e., segmentation of soft tissues in abdominal CT images [49] and global alignment of bone structures in pelvis x-ray images. Although the former has different target organs and imaging modality, the main ideas underneath are similar.

4.1 Segmentation of Soft Tissues in Abdominal CT Images

Automatic segmentation of soft tissues in abdominal CT images is carried out by non-rigid registration of 2-D atlas to target images. The atlas consists of a set of closed contours of the human body, liver, stomach, and spleen, which are manually segmented from a reference CT image given in [87]. As shown in Figure 4.1, the reference image is significantly different from the target image in terms of shapes and intensities of the body parts. Such differences are common in practical applications.

The segmentation algorithm consists of three stages: (1) Global alignment, (2) iterative local deformation, and (3) local refinement.

4.1.1 Global Alignment

This stage performs registration of the atlas to the target input image with *unknown correspondence*. First, the outer body contour of the target image (target contour) is

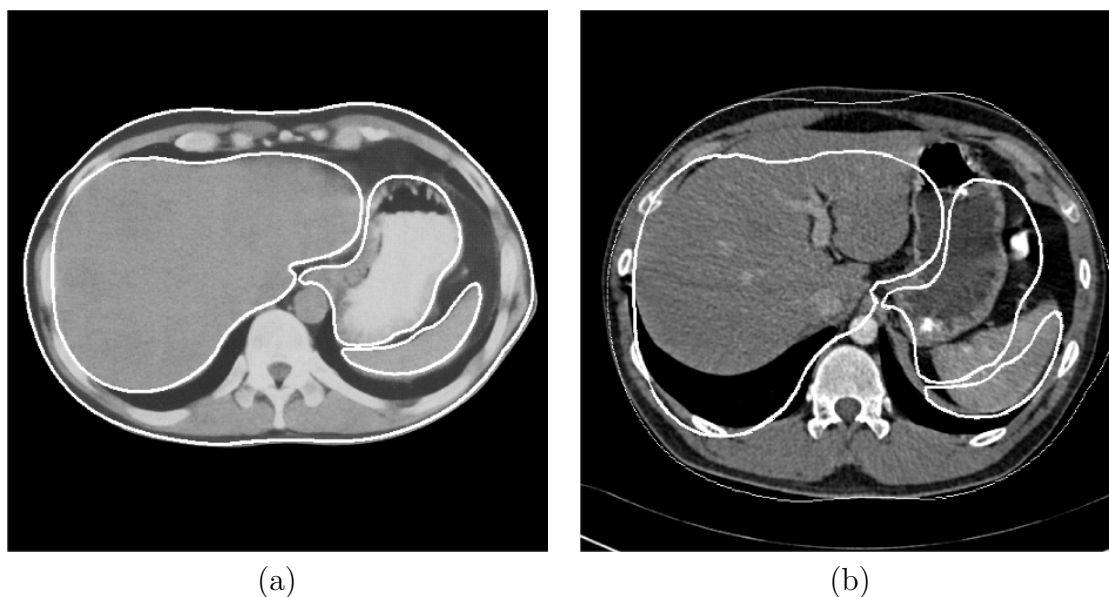


Figure 4.1: (a) Atlas contours (white curves) superimposed on the reference CT image taken from [87]. (b) Atlas registered onto a target image after global transformation.

extracted by straightforward contour tracing. Next, the outer body contour of the atlas (reference contour) is registered under affine transformation to the target contour using Iterative Closest Point algorithm. After registration, the correspondence between the reference and target contour points is known. Then, the affine transformation matrix between the reference and target contours is easily computed from the known correspondence by solving a system of over-constrained linear equations. This transformation matrix is then applied to the entire atlas to map the contours of the inner body parts to the target image.

4.1.2 Iterative Local Deformation

This stage iteratively applies local transformations to the individual body parts to bring their reference contours closer to the target contours. The idea is to search the local neighborhoods of reference contour points to find possible corresponding target contour points. To achieve this goal, it is necessary to use features that are invariant to image intensity because the reference and target images can have different intensities (as shown in Figure 4.1).

Let $N(p)$ denote the normal to the reference contour at point p , and $L(p)$ denote an ordered list of points $\{p_i\}$, $i = -n, \dots, 0, \dots, n$, lying on $N(p)$, with $p_0 = p$. Let $I(p_i)$ denote the intensity of point p_i . Then, the ordered list $D(p) = \{I(p_i) - I(p_{i+1})\}$, $i = -n, \dots, n - 1$, is the *intensity difference distribution* (IDD) at p along $N(p)$. IDD depends only on the local intensity difference, which does not differ as much as intensity across images. Thus, IDD is better than intensity for determining corresponding points between the images. In the same way, we can compute the IDD $D'(p')$ of an image point p' along a normal $N(p)$ of the reference contour and with respect to the target image intensities $I'(p'_i)$. In the current implementation, $n = 5$, i.e., the length of IDD is 10.

The local search for possible corresponding points is performed as follows. After coarse registration of the atlas and the reference image to the target image by global alignment. For each reference contour point p , a search is performed within a small neighborhood $U(p)$ centered at p and along the normal $N(p)$ for a target image point p' whose IDD $D'(p')$ is most similar to $D(p)$. The difference between $D(p)$ and $D'(p')$ is measured in terms of the Euclidean distance between them. The neighborhood $U(p)$ decreases quadratically over time so that the search process will converge. In the current implementation, the width of the search neighborhood is 100 at the first iteration.

After finding the best matching target image point p' of a reference contour point p , a verification procedure is performed. Shoot a ray from the centroid of the closed reference contour of p to p' . If the number of “white” pixels or “black” pixels along the ray in the target image exceeds a predefined threshold, then the point p' is discarded because the intensity of the desired body parts are gray. Otherwise, p' is regarded as a corresponding point of p .

Given the reference contour points p_i whose corresponding points p'_i are found, compute the affine transformation matrix that maps p_i to p'_i . Then, the matrix is applied to all reference contour points, including those whose corresponding points are not found.

The above local deformation is repeated iteratively for each closed contour of the body parts individually until the reference contours converge. Therefore, the reference contours of different body parts can be mapped to the corresponding target image contours through different affine transformation matrices that are appropriate for them.

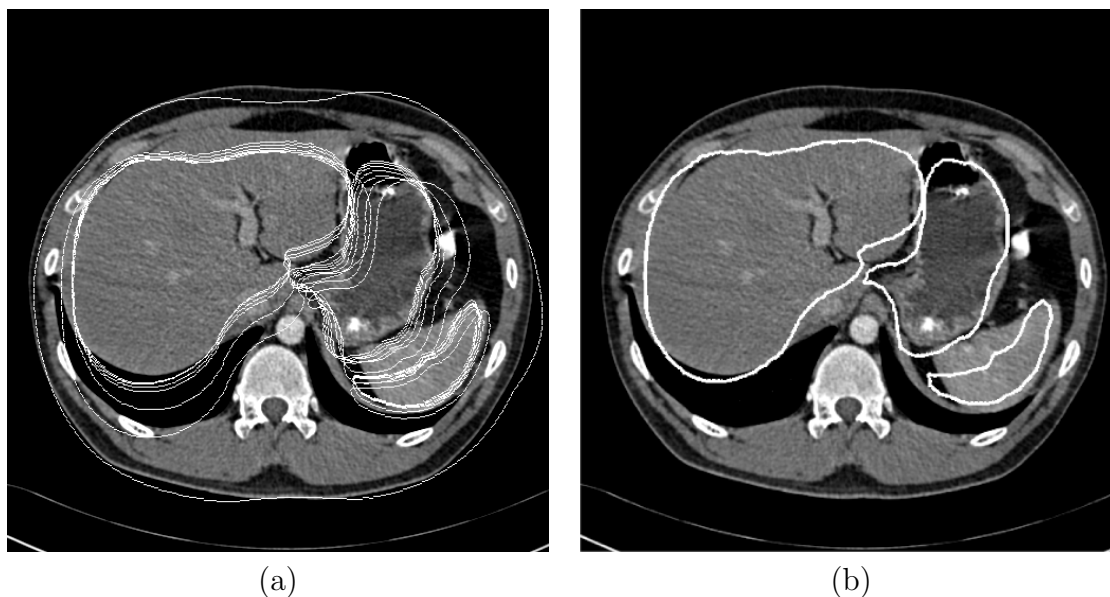


Figure 4.2: Iterative local transformation. (a) The white reference contours are iteratively transformed. (b) The result of iterative local transformation after convergence.

4.1.3 Local Refinement

The last stage performs local refinement of the atlas contour using active contour, i.e., snake algorithm [88] with Gradient Vector Flow (GVF) [29]. The original snake algorithm has the shortcoming of not being able to move into concave parts of the objects to be segmented. This is because there is no image forces outside the concave parts to attract the snake. GVF diffuses the gradient vectors of the edges outward, and uses the gradient vectors as the image forces to attract the snake into concave parts. Sample results are shown in Figure 4.3.

4.1.4 Experiments and Discussion

40 abdominal CT images (from slice 41 to 80) of 1mm thickness of a patient were used in the test. The accuracy of the segmentation result was measured in terms of the area of intersection between the target body part (that was obtained manually) and the segmented regions. This performance measure, called *similarity index* S , was proposed

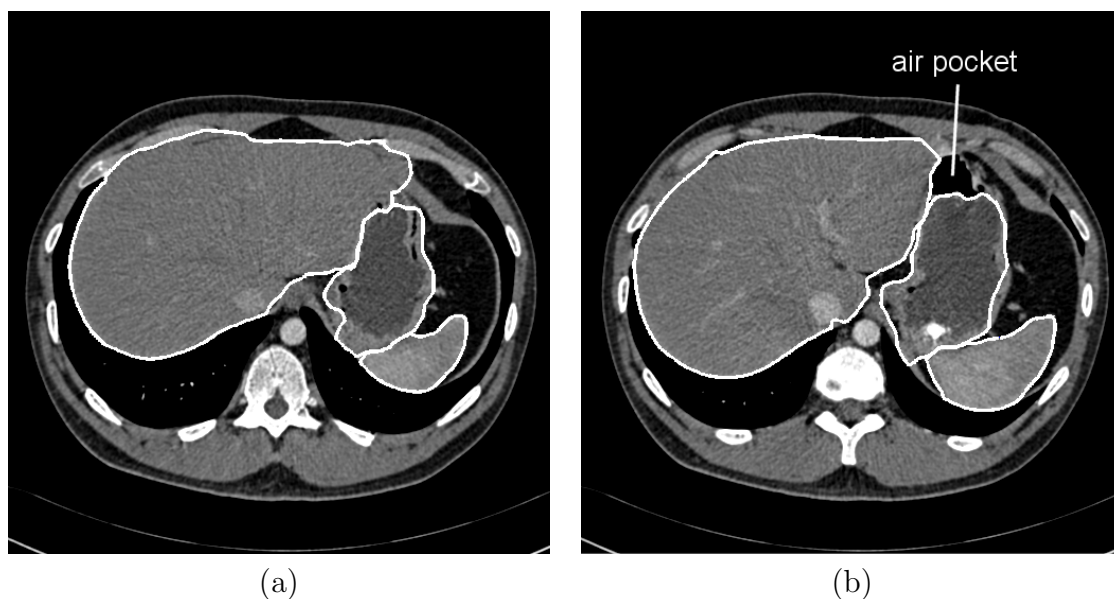


Figure 4.3: Sample results after refinement. (a) Good result. (b) Result affected by the air pocket inside the stomach.

by Zijdenbos et al. [89]:

$$S = 2 \frac{|A \cap B|}{|A| + |B|} \quad (4.1.1)$$

where A is the set of pixels of the body part in the target image and B that of the segmented region. When the segmented region coincide exactly with the target body part, $S = 1$.

Detailed segmentation performance of the algorithm is shown in Figure 4.4. The liver is well segmented and the algorithm's performance on liver is very stable (Figure 4.4(a)). The similarity indices are greater than 0.95 for slices 41 to 76 (Figure 4.4a). From slice 77 onward, the liver is split into two lobes, which is greatly different from that in the atlas image.

Figure 4.4(b) illustrates the average performance of the algorithm on segmenting the liver, spleen, and stomach. The similarity index is above 0.9 for slices 43 to 76. That is, with a single 2D atlas, the algorithm can successfully and accurately segment 34 slices of the abdominal CT volume.

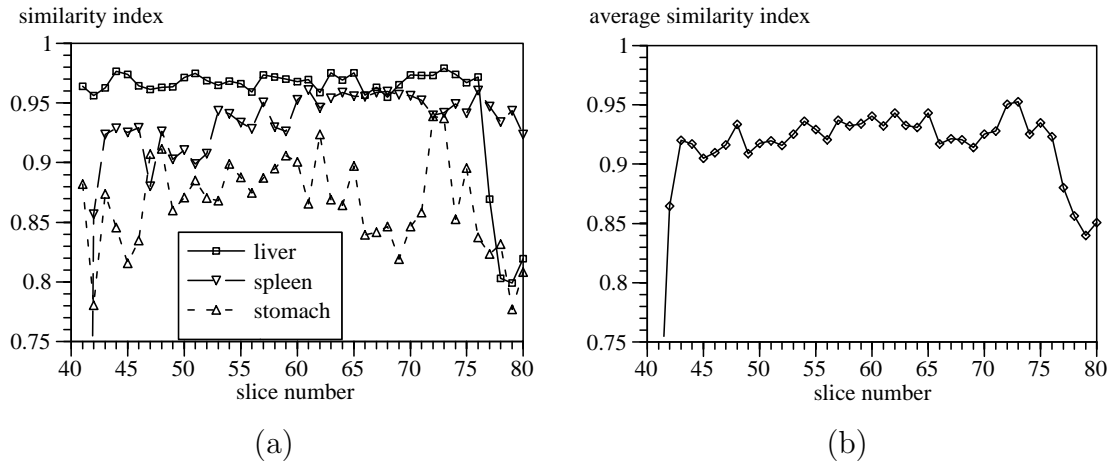


Figure 4.4: Test results. (a) Similarity indices of liver, spleen, and stomach. (b) Average similarity index.

4.2 Global Alignment of Bone Structures in Pelvis X-ray Images

In this preliminary work, the objective is to globally align an atlas of bone structure to pelvis x-ray images (Figure 4.5). The atlas image is randomly selected from a set of x-ray pelvis images. The contours of the bone structure, which consists of a pelvis bone and two femur bones, are manually delineated (white curves in Figure 4.5(a)).

The main idea of the algorithm is to locate the two femur bones first because they are often much clearer than the pelvis bone in the image, thus more likely to be detected. The pelvis bone is then translated, scaled and rotated according to the positions of the two femoral heads. The details of the algorithm are described below.

4.2.1 Segmentation Algorithm

The algorithm begins with a histogram equalization operation on the target images. Histogram equalization extends the gray levels of the image and boosts its contrast. This pre-processing step partially eliminates the intensity variations between images.

Next, the algorithm extracts low-level features in the equalized image. The low-level features used include edges, gradients and gradient directions because intensity alone is



Figure 4.5: Pelvis x-ray images. (a) Atlas x-ray image. The model contours are shown in white. (b) Target image.

not reliable as discussed in Chapter 3. The edge information is obtained by a combination of the Canny edge detector [7] and the Sobel edge operator. The Canny edge detector can produce edges with single pixel width. These edges are then filtered by the edge map produced by the Sobel edge operator so that weak edges are removed (Figure 4.6). From the resulting edge map (Figure 4.6(d)), a list of edge segments e_i are obtained by a simple edge tracing algorithm.

A normal global alignment technique is to transform the atlas contours to fit the edges in the target edge image. However, in this case, there exist many noise edges in the edge image. Registration of atlas contours to the target edge image is bound to be corrupted by the noise edges. The proposed algorithm performs the registration in the other direction, i.e., register the edge segments in the edge image to the atlas contours. This is based on the assumption that at least one edge segment in the edge map is very close to the the ideal boundary of the target femur. The assumption is reasonable due to the fact that the ideal boundaries of femurs, especially the shafts, are always clearly visible in the input image. Thus, they can be detected by an edge detection algorithm.

Each edge segment e_i is registered to a part of the atlas contour of the femur bone. The registration is performed using Iterative Closest Point (ICP) algorithm (Figure 4.7(b)). The distance function used in ICP incorporates both geometrical distance and gradient

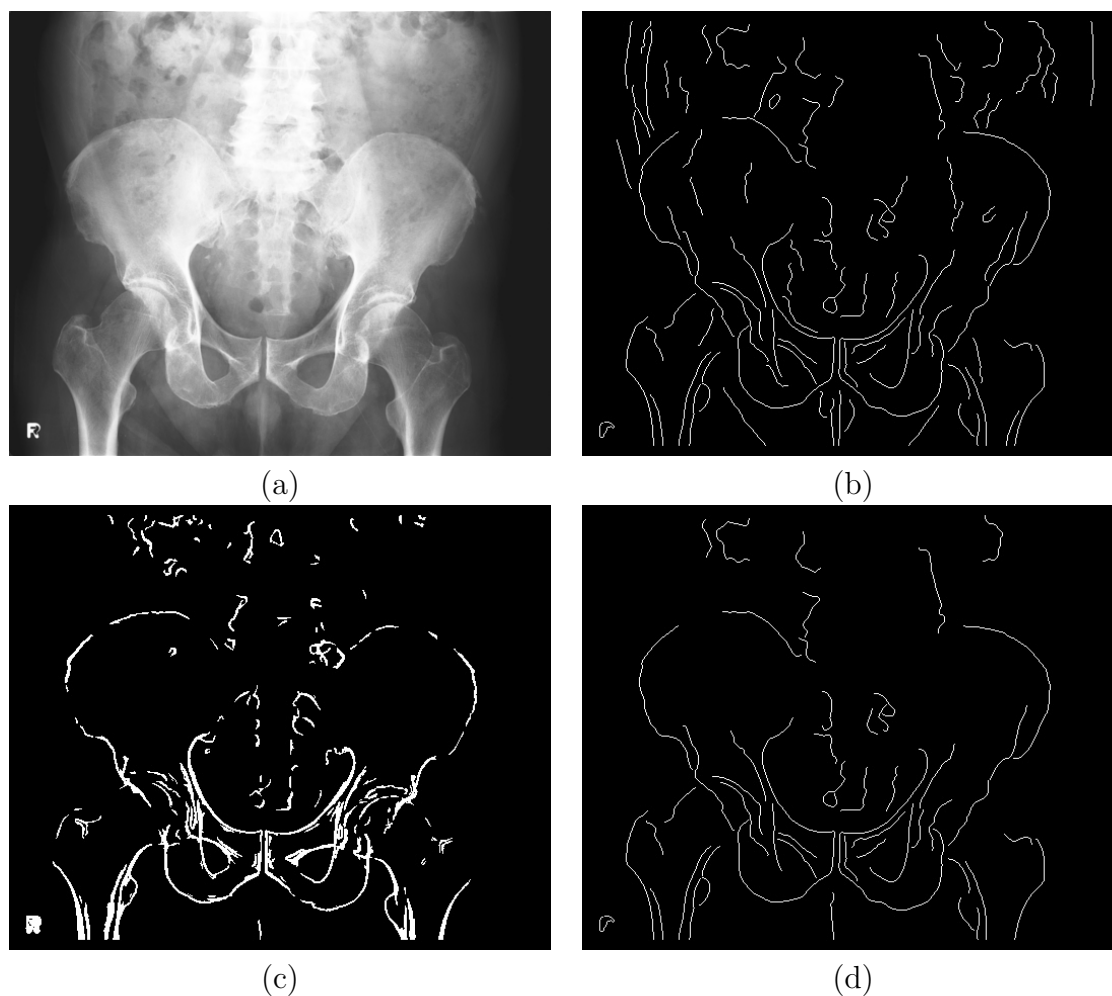


Figure 4.6: Edge extraction. (a) Input image. (b) Edges obtained by Canny edge detector. (c) Edges obtained by Sobel edge detector. (d) Edges in (b) filtered by (c) according to the edge strength.

direction information. The transformation used is rigid, which is to ensure that the scale of e_i remains fixed. After ICP, a rigid transformation T_i is obtained for each e_i . The atlas contour is then registered to the edge segment e_i based on the inverse of the transformation T_i , i.e., T_i^{-1} (Figure 4.7(c), 4.8). After registration to all the edge segments, a set of candidate transformations T_i^{-1} is obtained. Among these candidates, the optimal transformation T_o is selected based on minimizing a cost function describing the closest distance between the transformed atlas contour and the edge points in the Sobel edge map.

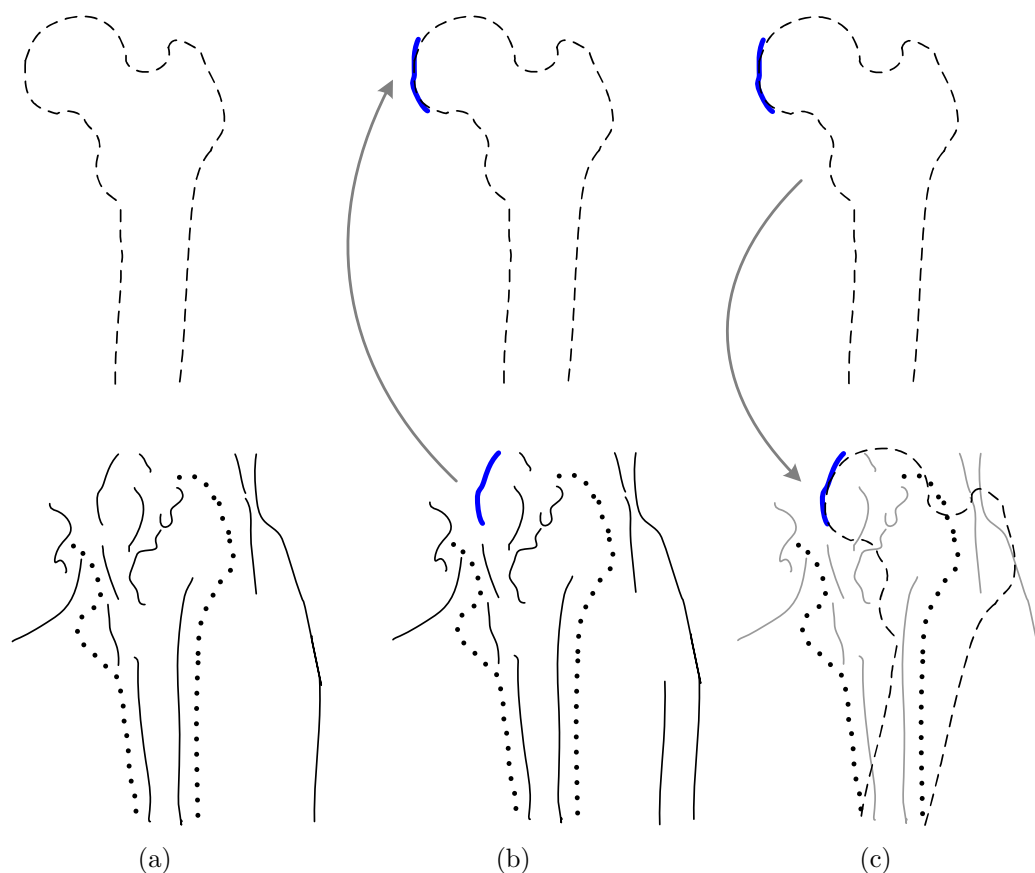


Figure 4.7: Global alignment algorithm. (a) The atlas contour (dashed line) and the target edge segments (solid line). The edge segments represented in dot line correspond to the boundary of the femur in the image. The black edge segments (solid line) are noise. (b) Each edge segment (thick solid line) is registered to the atlas contour. (c) The atlas contour is transformed back to register to the edge segments.

After determining the optimal transformations of both the left and right femur bones, the locations of the two femoral heads are found. The pelvis bone is connected to the femurs at the femoral heads. Therefore, based on the positions of the femoral heads, the pelvis can be properly scaled, rotated and translated.

4.2.2 Experiments and Discussion

A test was performed on 45 pelvis x-ray images of size 534×440 pixels. Results of global alignment are inspected visually. Among all the 45 test images, 37 images have relatively

good results (Figure 4.9). The remaining 8 images have poorer results, in which the worst cases are shown in Figure 4.10. The poorer results may be due to the noise edges in the image that corrupt the computation of the optimal transformation T_o .

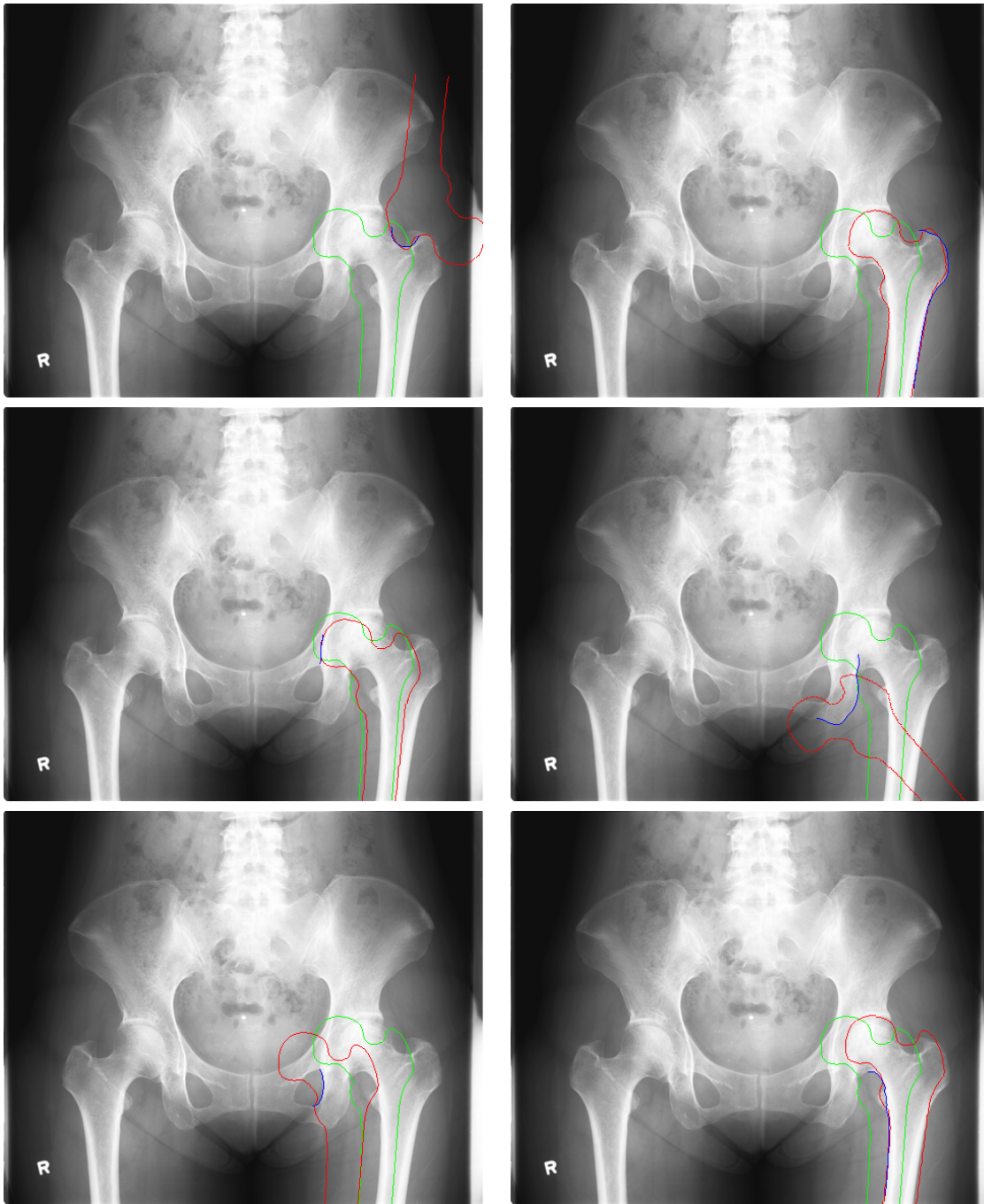


Figure 4.8: Registration of atlas contour to different edge segments in an input image. Atlas contours are marked in green. Edges in the image are marked in blue. Transformed atlas contours are marked in red.

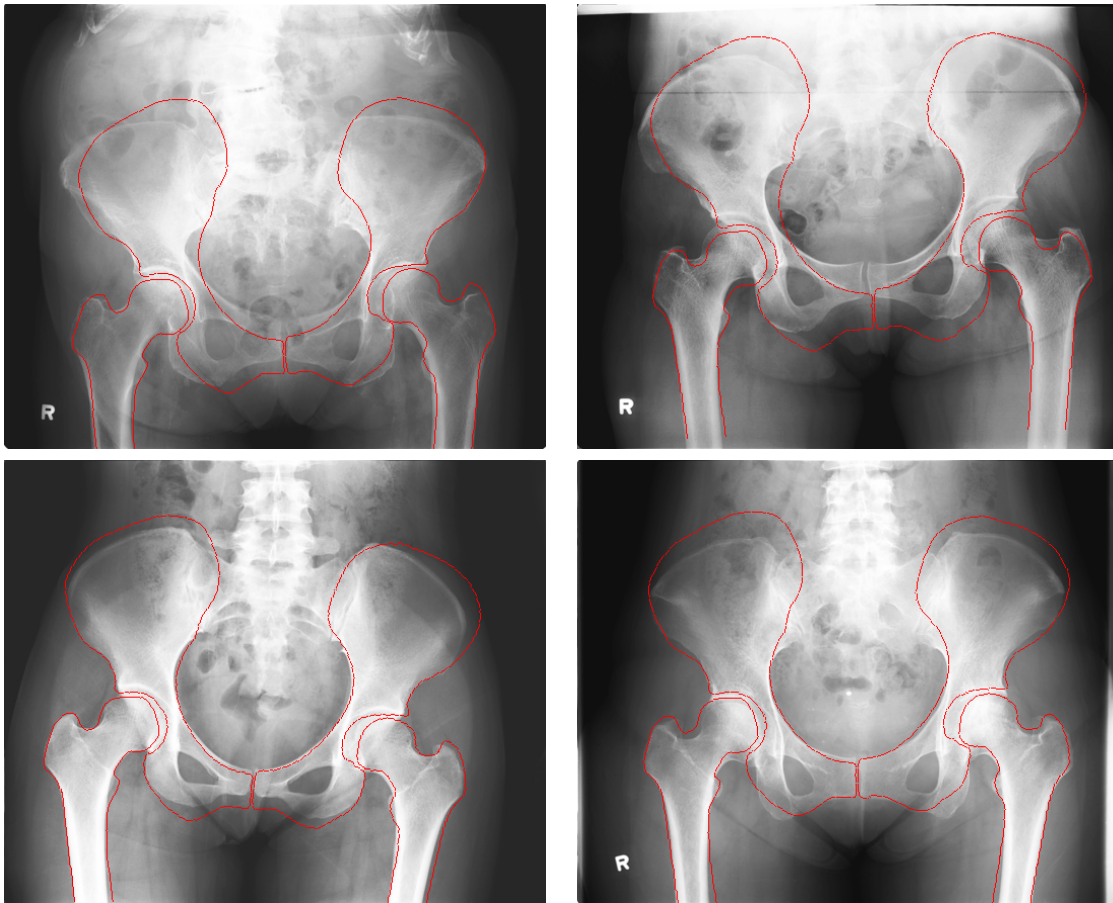


Figure 4.9: Sample good results of global alignment. Registered atlas contours are shown in red.

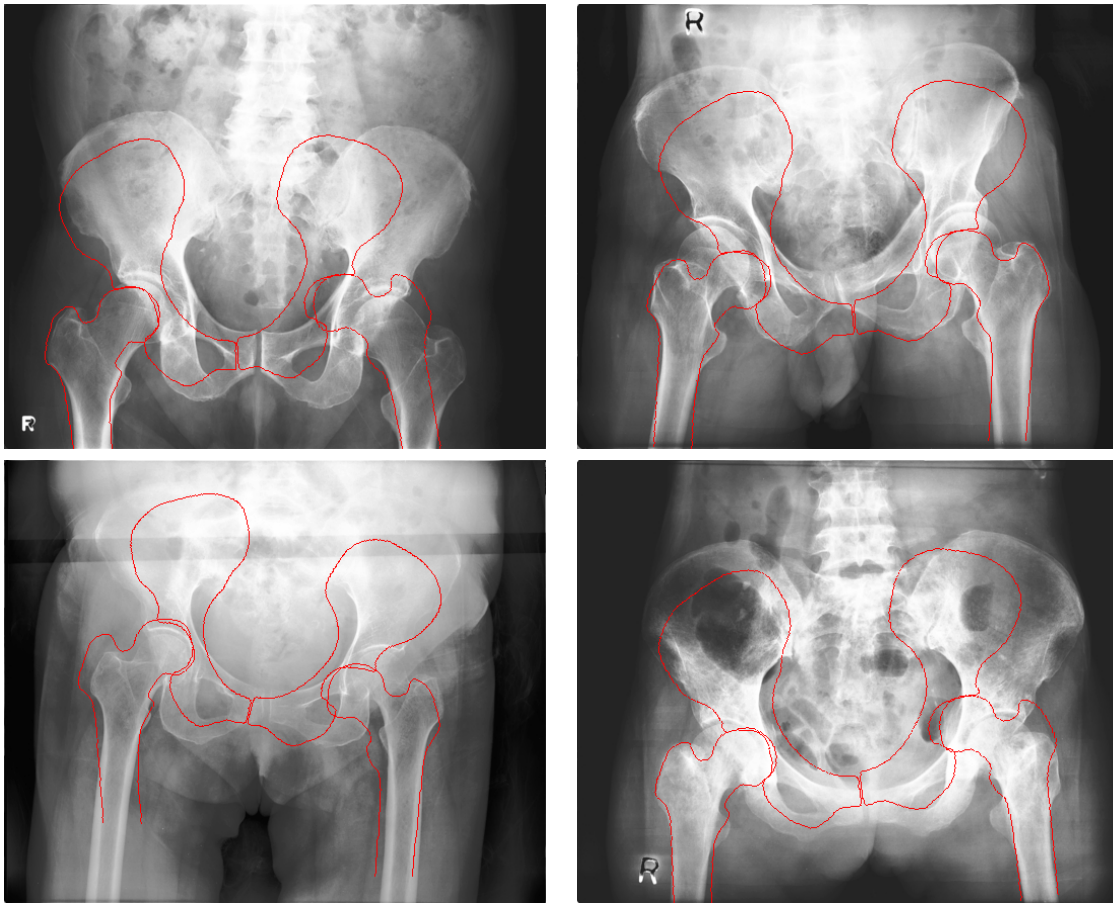


Figure 4.10: Sample poorer results of global alignment. Registered atlas contours are shown in red.

Chapter 5

Conclusions

In this thesis proposal, a thorough review of the general medical image segmentation algorithms, particularly atlas-based medical image segmentation algorithms and x-ray image segmentation algorithms, is presented. General segmentation algorithms are categorized into six classes, namely thresholding, region-based, edge-based, graph-based, classification-based and deformable models. Apart from deformable models, they usually work on either individual pixels or local image patches, and are very sensitive to noise. In comparison, deformable models perform segmentation by fitting a connected contour to the features (usually edges) in the image. Therefore, they are less sensitive to noise.

Atlas-based segmentation algorithms consist of two major steps, namely global alignment and local refinement. Global alignment globally registers the atlas to the target image to determine an approximation of the position, scale and orientation of the atlas. Local refinement registers the atlas contours to the object boundaries in the target image as accurately as possible. Since the atlas contains domain knowledge, it is more promising for solving the complex problem of segmenting bone structures in x-ray images.

Currently, most x-ray image segmentation methods rely on general algorithms. Atlas-based segmentation of x-ray images is proposed in [85]. However, their global alignment algorithm using shape context as the feature is not robust against noise. The use of active shape model for local refinement may not extract the bone boundaries accurately. In addition, articulation is not considered explicitly in the segmentation process. In conclusion, segmentation of bone structures in x-ray images is not well studied.

The research plan decomposes the complex segmentation problem into three parts:

feature selection, global alignment and local refinement. Two pieces of preliminary work have been accomplished: segmentation of soft tissues in CT images and global alignment of bone structures in x-ray images. According to the preliminary work, the feature selection part is almost completed. The global alignment results show that the algorithm is promising but needs to be improved so that it can perform reliably on all test images. Moreover, articulation of bones needs to be incorporated into the global alignment process. Local refinement remains to be done. The algorithm proposed for segmenting soft tissues in CT images is promising, and can provide ideas for local refinement.

Bibliography

- [1] D. L. Pham, C. Xu, and J. L. Prince, “A survey of current methods in medical image segmentation,” Department of Electrical and Computer Engineering, The Johns Hopkins University, Tech. Rep., 1998.
- [2] J. Rogowska, “Overview and fundamentals of medical image segmentation,” in *Handbook of Medical Imaging, Processing and Analysis*, I. N. Bankman, Ed. Academic Press, 2000, ch. 5, pp. 69–85.
- [3] M. Sezgin and B. Sankur, “Survey over image thresholding techniques and quantitative performance evaluation,” *Journal of Electronic Imaging*, vol. 13, no. 1, pp. 146–165, January 2004.
- [4] R. C. Gonzalez and R. E. Woods, *Digital Image Processing*. Prentice Hall, 2001.
- [5] A. Goshtasby and D. A. Turner, “Segmentation of cardiac cine MR images for extraction of right and left ventricular chambers,” *IEEE Transactions on Medical Imaging*, vol. 14, no. 1, pp. 56–64, March 1995.
- [6] M. Bomans, K.-H. Höhne, U. Tiede, and M. Riemer, “3-D segmentation of MR images of the head for 3-D display,” *IEEE Transactions on Medical Imaging*, vol. 9, no. 2, pp. 177–183, June 1990.
- [7] J. Canny, “A computational approach to edge detection,” *IEEE Transactions on Pattern Analysis and Machine Intelligence*, vol. 8, no. 6, pp. 679–698, November 1986.
- [8] C. Harris and M. Stephens, “A combined corner and edge detector,” in *Proceedings of the 4th ALVEY Vision Conference*, 1988, pp. 147–151.

-
- [9] L. O’Gorman and A. C. Sanderson, “The converging squares algorithm: An efficient multidimensional peak picking method,” in *International Conference on Acoustics, Speech, and Signal Processing*, vol. 8, April 1983, pp. 112–115.
- [10] R. Adams and L. Bischof, “Seeded region growing,” *IEEE Transaction on Pattern Analysis and Machine Intelligence*, vol. 16, no. 6, pp. 641–647, June 1994.
- [11] X. Yu, J. Ylä-Jääski, O. Huttunen, T. Vehkomäki, O. Sipilä, and T. Katila, “Image segmentation combining region growing and edge detection,” in *Pattern Recognition, International Conference on*, vol. III, April 1992, pp. 481–484.
- [12] R. Pohle and K. Toennies, “Segmentation of medical images using adaptive region growing,” in *Proc. SPIE (Medical Imaging 2001)*, 2001.
- [13] S. Beucher and C. Lantuéjoul, “Use of watersheds in contour detection,” in *Proc. International Workshop on Image Processing, Real-Time Edge and Motion Detection/Estimation*, September 1979.
- [14] J. Serra, *Image Analysis and Mathematical Morphology*. Academic Press, 1982.
- [15] J. B. Roerdink and A. Meijster, “The watershed transform: Definitions, algorithms and parallelization strategies,” *Fundamenta Informaticae*, vol. 41, 2001.
- [16] V. Grau, A. Mewes, M. Alcañiz, R. Kikinis, and S. Warfield, “Improved watershed transform for medical image segmentation using prior information,” *IEEE Transaction on Medical Imaging*, vol. 23, no. 4, pp. 447–458, 2004.
- [17] L. Najman and M. Schmitt, “Geodesic saliency of watershed contours and hierarchical segmentation,” *Pattern Analysis and Machine Intelligence, IEEE Transactions on*, vol. 18, Dec 1996.
- [18] S. Wegner, T. Harms, H. Oswald, and E. Fleck, “The watershed transformation on graphs for the segmentation of CT images,” in *Proceedings of the 13th International Conference on Pattern Recognition*, August 1996, pp. 498–502.
- [19] Z. Wu and R. Leahy, “An optimal graph theoretic approach to data clustering: Theory and its application to image segmentation,” *IEEE Transactions on Pattern Analysis and Machine Intelligence*, vol. 15, no. 11, pp. 1101–1113, November 1993.
-

- [20] J. Shi and J. Malik, “Normalized cuts and image segmentation,” *IEEE Transactions on Pattern Analysis and Machine Intelligence*, vol. 22, no. 8, pp. 888–905, August 2000.
- [21] S. Wang and J. M. Siskind, “Image segmentation with ratio cut,” *IEEE Transactions on Pattern Analysis and Machine Intelligence*, vol. 25, no. 6, pp. 675–690, June 2003.
- [22] Y. Boykov and M.-P. Jolly, “Interactive graph cuts for optimal boundary & region segmentation of objects in N-D images,” in *Proceedings of International Conference on Computer Vision*, 2001, pp. 105–112.
- [23] X. Ren and J. Malik, “Learning a classification model for segmentation,” in *International Conference on Computer Vision*, Nice, France, October 2003.
- [24] M. S. Brown, M. F. Mcnitt-Gray, J. G. G. Nicholas J. Mankovich, J. Hiller, L. S. Wilson, and D. R. Aberle, “Method for segmenting chest CT image data using an anatomical model: Preliminary results,” *IEEE Transactions on Medical Imaging*, vol. 16, no. 6, pp. 828–839, 1997.
- [25] J. Feng, W.-C. Lin, and C.-T. Chen, “Epicardial boundary detection using fuzzy reasoning,” *Medical Imaging, IEEE Transactions on*, vol. 10, no. 2, pp. 187–199, June 1991.
- [26] D. L. Toulson and J. F. Boyce, “Segmentation of MR image using neural nets,” in *Image and Vision Computing*, vol. 10, 1992, pp. 324–328.
- [27] M. Kass, A. Witkin, and D. Terzopoulos, “Snakes: Active contour models,” *Int’l J. Computer Vision*, pp. 321–331, 1987.
- [28] M. S. Atkins and B. T. Mackiewicz, “Fully automated hybrid segmentation of the brain,” in *Handbook of Medical Imaging, Processing and Analysis*, I. N. Bankman, Ed. Academic Press, 2000, ch. 11, pp. 171–183.
- [29] C. Xu and J. L. Prince, “Snakes, shapes, and gradient vector flow,” *IEEE Transaction on Image Processing*, vol. 7, no. 3, March 1998.

-
- [30] J. A. Sethian, *Level Set Methods and Fast Marching Methods. Evolving Interfaces in Computational Geometry, Fluid Mechanics, Computer Vision, and Materials Science*. Cambridge University Press, 1999.
- [31] —, “Tracking interfaces with level sets,” *American Scientist*, May–June 1997.
- [32] R. Malladi, J. A. Sethian, and B. C. Vemuri, “Shape modeling with front propagation: A level set approach,” *IEEE Transactions on Pattern Analysis and Machine Intelligence*, vol. 17, no. 2, pp. 158–175, February 1995.
- [33] M. Droske, B. Meyer, M. Rumpf, and K. Schaller, “An adaptive level set method for medical image segmentation,” in *Proc. of the Annual Symposium on Information Processing in Medical Imaging*, 2001.
- [34] J. Yang, L. H. Staib, and J. S. Duncan, “Neighbor-constrained segmentation with level set based 3-d deformable models,” *IEEE Transactions on Medical Imaging*, 2004.
- [35] T. F. Cootes, A. Hill, C. J. Taylor, and J. Haslam, “The use of active shape models for locating structures in medical images,” *Image and Vision Computing*, vol. 12, no. 6, pp. 355–366, July 1994.
- [36] T. F. Cootes, G. J. Edwards, and C. J. Taylor, “Active appearance models,” in *Proc. European Conference on Computer Vision*, vol. 2, 1998, pp. 484–498.
- [37] A. Hill, C. J. Taylor, and T. Cootes, “Object recognition by flexible template matching using genetic algorithms,” in *European Conference on Computer Vision*, May 1992, pp. 852–856.
- [38] T. F. Cootes and C. J. Taylor, “Statistical models of appearance for computer vision,” *Imaging Science and Biomedical Engineering*, Manchester M13 9PT, U.K., Tech. Rep., March 2004.
- [39] Y. Wang and L. H. Staib, “Boundary finding with correspondence using statistical shape models,” in *Computer Vision and Pattern Recognition*, June 1998, pp. 338–345.

- [40] S. S. Gleason, H. Sari-Sarraf, M. A. Abidi, O. Karakashian, and F. Morandi, “A new deformable model for analysis of X-Ray CT images in preclinical studies of mice for polycystic kidney disease,” *IEEE Transactions on Medical Imaging*, vol. 21, no. 10, pp. 1302–1309, October 2002.
- [41] G. B. Aboutanos, J. Nikanne, N. Watkins, and B. M. Dawant, “Model creation and deformation for the automatic segmentation of the brain in MR images,” *IEEE Transaction on Biomedical Engineering*, vol. 46, no. 11, pp. 1346–1356, 1999.
- [42] P.-Y. Bondiau, G. Malandain, S. Chanalet, P.-Y. Marcy, J.-L. Habrand, F. Fauchon, P. Paquis, A. Courdi, O. Commowick, I. Rutten, and N. Ayache, “Atlas-based automatic segmentation of mr images: Validation study on the brainstem in radiotherapy context,” *International Journal of Radiation Oncology Biology Physics*, vol. 61, no. 1, pp. 289–298, January 2005.
- [43] P. Cachier and X. Pennec, “3D non-rigid registration by gradient descent on a gaussian-windowed similarity measure using convolutions,” in *Mathematical Methods in Biomedical Image Analysis*, June 2000, pp. 182–189.
- [44] M. Chen, T. Kanade, H. A. Rowley, and D. Pomerleau, “Quantitative study of brain anatomy,” in *Mathematical Methods in Biomedical Image Analysis*, June 1998, pp. 84–92.
- [45] F. S. Cohen and C. Pintavirooj, “Invariant surface alignment in the presence of affine and some nonlinear transformations,” *Medical Image Analysis*, vol. 8, no. 2, pp. 151–164, June 2004.
- [46] M. B. Cuadra, O. Cuisenaire, R. Meuli, and J. P. Thiran, “Automatic segmentation of internal structures of the brain in mr images using a tandem of affine and non-rigid registration of an anatomical brain atlas,” in *Image Processing*, Oct. 2001, pp. 1083–1086.
- [47] M. B. Cuadra, C. Pollo, A. Bardera, O. Cuisenaire, J.-G. Villemure, and J.-P. Thiran, “Atlas-based segmentation of pathological MR brain images using a model of lesion growth,” *IEEE Transaction on Medical Imaging*, vol. 23, no. 10, pp. 1301–1314, 2004.

- [48] B. M. Dawant, S. L. Hartmann, J. P. Thirion, F. Maes, D. Vandermeulen, and P. Demaerel, “Automatic 3-D segmentation of internal structures of head in MR images using a combination of similarity and free-form transformations: Part I, methodology and validation on normal subjects,” *IEEE Trans. on Medical Imaging*, vol. 18, no. 10, pp. 909–916, 1999.
- [49] F. Ding, W. K. Leow, and S.-C. Wang, “Segmentation of 3D CT volume images using a single 2D atlas,” in *Proc. First International Workshop on Computer Vision for Biomedical Image Applications (CVBIA 2005)*, 2005, pp. 459–468.
- [50] V. Duay, N. Houhou, and J.-P. Thiran, “Atlas-based segmentation of medical images locally constrained by level sets,” Signal Processing Institute (ITS), Ecole Polytechnique Fédérale de Lausanne (EPFL), Tech. Rep., 2005.
- [51] K. A. Ganser, H. Dickhaus, R. Metzner, and C. R. Wirtz, “A deformable digital brain atlas system according to talairach and tournoux,” *Medical Image Analysis*, vol. 8, no. 1, pp. 3–22, March 2004.
- [52] S. L. Hartmann, M. H. Parks, P. R. Martin, and B. M. Dawant, “Automatic 3-D segmentation of internal structures of head in MR images using a combination of similarity and free-form transformations: Part II, validation on severely atrophied brains,” *IEEE Trans. on Medical Imaging*, vol. 18, no. 10, pp. 917–926, 1999.
- [53] M. Lorenzo-Valdés, G. I. Sanchez-Ortiz, R. Mohiaddin, and D. Rueckert, “Atlas-based segmentation and tracking of 3D cardiac MR images using non-rigid registration,” in *International Conference on Medical Image Computing and Computer-Assisted Intervention*, 2002, pp. 642–650.
- [54] M. G. Linguraru, M. Ángel González Ballester, and N. Ayache, “Deformable atlases for the segmentation of internal brain nuclei in magnetic resonance imaging,” *Acta Universitatis Cibiniensis, Technical Series*, 2005, to appear.
- [55] D. Rueckert, G. I. Sanchez-Ortiz, M. Lorenzo-Valdés, R. Chandrashekhara, and R. Mohiaddin, “Non-rigid registration of cardiac MR: Application to motion modelling and atlas-based segmentation,” in *IEEE International Symposium on Biomedical Imaging*, 2002.

- [56] S. Sandor and R. Leahy, “Surface-based labeling of cortical anatomy using a deformable atlas,” *IEEE Transactions on Medical Imaging*, vol. 16, no. 1, pp. 41–54, February 1997.
- [57] D. Shen and C. Davatzikos, “An adaptive-focus deformable model using statistical and geometric information,” *IEEE Transactions on Pattern Analysis and Machine Intelligence*, vol. 22, no. 8, pp. 906–913, August 2000.
- [58] D. Shen, E. H. Herskovits, and C. Davatzikos, “An adaptive-focus statistical shape model for segmentation and shape modeling of 3-D brain structures,” *IEEE Transactions on Medical Imaging*, vol. 20, no. 4, pp. 257–270, April 2001.
- [59] D. Shen, Z. Lao, J. Zeng, W. Zhang, I. A. Sesterhenn, L. Sun, J. W. Moul, E. H. Herskovits, G. Fichtinger, and C. Davatzikos, “Optimized prostate biopsy via a statistical atlas of cancer spatial distribution,” *Medical Image Analysis*, vol. 8, no. 2, pp. 139–150, June 2004.
- [60] B. C. Vemuri, Y. C. J. Ye, and C. M. Leonard, “Image registration via level-set motion: Applications to atlas-based segmentation,” *Medical Image Analysis*, vol. 7, no. 1, pp. 1–20, March 2003.
- [61] Y. Chen, F. Huang, H. D. Tagare, M. Rao, D. Wilson, and E. A. Geiser, “Using prior shape and intensity profile in medical image segmentation,” in *Proceedings of Ninth IEEE International Conference on Computer Vision*, 2003.
- [62] M. Lorenzo-Valdés, D. Rueckert, R. Mohiaddin, and G. I. Sanchez-Ortiz, “Segmentation of cardiac MR images using the em algorithm with 4D probabilistic atlas and a global connectivity filter,” in *International Conference of the IEEE Engineering in Medicine and Biology Society*, 2003.
- [63] M. Lorenzo-Valdés, G. I. Sanchez-Ortiz, A. G. Elkington, R. H. Mohiaddin, and D. Rueckert, “Segmentation of 4D cardiac MR images using a probabilistic atlas and the EM algorithm,” *Medical Image Analysis*, vol. 8, pp. 255–265, 2004.
- [64] H. Park, P. H. Bland, and C. R. Meyer, “Construction of an abdominal probabilistic atlas and its application in segmentation,” *IEEE Trans. on Medical Imaging*, vol. 22, no. 4, pp. 483–492, 2003.

- [65] M. Prastawa, J. H. Gilmore, W. Lin, and G. Gerig, “Automatic segmentation of MR images of the developing newborn brain,” *Medical Image Analysis*, 2005.
- [66] I. Sluimer, M. Prokop, and B. van Ginneken, “toward automated segmentation of the pathological lung in CT,” *IEEE Transactions on Medical Imaging*, vol. 24, no. 8, pp. 1025–1038, August 2005.
- [67] M. Straka, A. L. Cruz, A. Köchl, M. Sránek, M. E. Gröller, and D. Fleischmann, “3d watershed transform combined with a probabilistic atlas for medical image segmentation,” in *MIT 2003*, 2003, pp. <http://www.cg.tuwien.ac.at/research/publications/2003/Straka-2003-3DW/>
- [68] S. L. Hartmann, M. H. Parks, H. Schlack, W. Riddle, R. R. Price, P. R. Martin, and B. M. Dawant, “Automatic computation of brain and cerebellum volumes in normal subjects and chronic alcoholics,” in *IPMI*, A. Kuba, M. Sámal, and A. Todd-Pokropek, Eds., vol. 1613. Springer, 1999, pp. 430–435.
- [69] J. P. Thirion, “Image matching as a diffusion process: An analogy with maxwell’s demons,” *Medical Image Analysis*, vol. 2, no. 3, pp. 243–260, 1998.
- [70] P. Cachier, E. Bardinet, D. Dormont, X. Pennec, and N. Ayache, “Iconic feature based nonrigid registration: The PASHA algorithm,” *CVIU — Special Issue on Nonrigid Registration*, vol. 89, no. 2-3, pp. 272–298, Feb.-march 2003.
- [71] P. J. Rousseeuw and K. V. Driessen, “A fast algorithm for the minimum covariance determinant estimator,” *Technometrics*, vol. 41, no. 3, pp. 212–223, August 1999.
- [72] G. K. Manos, A. Y. Cairns, I. W. Rickets, and D. Sinclair, “Segmenting radiographs of the hand and wrist,” *Computer Methods and Programs in Biomedicine*, vol. 43, no. 3-4, pp. 227–237, June 1993.
- [73] S. S.-A. El-Feghi, I. and Huang, M.A., and M. Ahmadi, “X-ray image segmentation using auto adaptive fuzzy index measure,” in *MWSCAS '04. The 2004 47th Midwest Symposium on Circuits and Systems*, vol. 3, 2004, pp. 499–502.
- [74] M. F. McNitt-Gray, H. K. Huang, and J. W. Sayre, “Feature selection in the pattern classification problem of digital chest radiograph segmentation,” *IEEE Transactions on Medical Imaging*, vol. 14, no. 3, pp. 537–547, September 1995.

- [75] Z. Yue, A. Goshtasby, and L. V. Ackerman, “Automatic detection of rib borders in chest radiographs,” *IEEE Transactions on Medical Imaging*, vol. 14, no. 3, pp. 525–536, September 1995.
- [76] V. Caselles, R. Kimmel, and G. Sapiro, “Geodesic active contours,” in *ICCV*, 1995, pp. 694–699.
- [77] Y. Jiang and P. Babyn, “X-ray bone fracture segmentation by incorporating global shape model priors into geodesic active contours,” in *Proceedings of the 18th International Congress and Exhibition*, vol. 1268, June 2004, pp. 219–224.
- [78] H. Chen and A. K. Jain, “Tooth contour extraction for matching dental radiographs,” in *Proc. International Conference on Pattern Recognition*, 2004, pp. 522–525.
- [79] Y. Chen, X. Ee, W. K. Leow, and T. S. Howe, “Automatic extraction of femur contours from hip x-ray images,” in *Proc. First International Workshop on Computer Vision for Biomedical Image Applications (CVBIA 2005)*, 2005, pp. 200–209.
- [80] G. Behiels, D. Vandermeulen, F. Maes, P. Suetens, and P. Dewaele, “Active shape model-based segmentation of digital x-ray images,” in *Proceedings of the Second International Conference on Medical Image Computing and Computer-Assisted Intervention*, 1999, pp. 128–137.
- [81] L. Ballerini and L. Bocchi, “Bone segmentation using multiple communicating snakes,” in *SPIE International Symposium Medical Imaging*, 2003.
- [82] R. Bernard, B. Likar, and F. Pernus, “Segmenting articulated structures by hierarchical statistical modeling of shape, appearance and topology,” in *Medical Image Computing and Computer Assisted Intervention - 4th MICCAI*, 2001, pp. 499–506.
- [83] C. Vinhais and A. Campilho, “Genetic model-based segmentation of chest x-ray images using free form deformations,” in *Image Analysis and Recognition: Second International Conference, ICIAR 2005*, 2005.
- [84] T. W. Sederberg and S. R. Parry, “Free-form deformation of solid geometric models,” in *ACM SIGGRAPH Computer Graphics*, vol. 20, 1986, pp. 151–160.

- [85] N. Boukala, E. Favier, B. Laget, and P. Radeva, “Active shape model based segmentation of bone structures in hip radiographs,” in *Proceedings of IEEE International Conference on Industrial Technology*, 2004, pp. 1682–1687.
- [86] S. Belongie, J. Malik, and J. Puzicha, “Shape context: A new descriptor for shape matching and object recognition,” in *NIPS*, 2000, pp. 831–837.
- [87] P. Fleckenstein and J. T. Jensen, *Anatomy in Diagnostic Imaging*. Munksgaard, 1993.
- [88] M. Kass, A. Witkin, and D. Terzopoulos, “Snakes: active contour models,” *Int. J. of Computer Vision*, vol. 1, no. 4, pp. 321–331, 1987.
- [89] A. P. Zijdenbos, B. M. Dawant, R. A. Margolin, and A. C. Palmer, “Morphometric analysis of white matter lesions in MR images: Method and validation,” *IEEE Trans. on Medical Imaging*, vol. 13, no. 4, pp. 716–724, 1994.